Wavelength-scaled laser filamentation in solids and plasma-assisted subcycle light-bullet generation in the long-wavelength infrared

Rostislav I. Grynko, Garima C. Nagar, and Bongggu Shim

Phys. Rev. A **98**, 023844 — Published 23 August 2018

DOI: 10.1103/PhysRevA.98.023844

Wavelength-scaled laser filamentation in solids and plasma-assisted sub-cycle light bullet generation in the long-wavelength infrared

Rostislav I. Grynko, Garima C. Nagar, and Bonggu Shim[*]
Department of Physics, Applied Physics, and Astronomy, Binghamton University,
State University of New York, Binghamton, New York 13902, USA

We theoretically investigate mid- and long-wavelength infrared laser filamentation in solids, revealing extreme self-steepening and optical shock, multi-octave spanning supercontinuum generation, and most importantly sub-cycle light bullet generation. Light bullet generation in solids at long wavelengths depends critically on plasma, which is in sharp contrast to that in air where the arrest of collapse for light bullet generation is dominated by radiation loss. Our method for sub-cycle light bullet generation in solids at long wavelengths can open new possibilities for extreme ultrafast nonlinear optics including high-order harmonic and attosecond pulse generation.

PACS numbers: 42.65 Jx, 42.65 Re, 42.65 Sf

Laser filamentation, which is self-guidance of a high-intensity, ultrashort laser pulse, is a remarkable nonlinear optical phenomenon because of its rich and novel science, and many practical applications [1–4]. Although laser filamentation has been studied mainly with near-infrared and visible wavelengths, recent advances of laser technology in the mid-infrared (mid-IR) and even the long-wavelength infrared (LWIR) [5–9] enable investigation of unexplored wavelength regimes of laser filamentation and nonlinear optics. For example, with longer wavelengths, beams can deliver significantly more energy due to the λ^2 scaling of the critical power for self-focusing [10], where λ is the wavelength. Moreover, the scaling of electron ponderomotive energy with λ^2 [11, 12] makes mid-IR/LWIR useful for high-order harmonic generation (HHG) [13–15] and zeptosecond pulse generation [16].

Recent theoretical work on mid-IR pulse propagation in gases has predicted that at long wavelengths, self-compression and self-steepening give rise to single-cycle pulses and a supercontinuum that spans multiple octaves [17]. Mid-IR/LWIR ultrashort pulses have been shown to exhibit drastically different propagation dynamics than pulses in the near-IR, including optical shock formation [17–20], accelerated third-harmonic generation via vibrational excitation of N_2 and O_2 [21], extended and smooth filamentation [22, 23], and a significant defocusing contribution due to many-body effects, leading to long-range self-channeling [24]. Furthermore, Panagiotopoulos *et al.* [18] have theoretically demonstrated long-range, high-power 3-D spatio-temporal solitary waves (i.e., light bullets [25, 26]) in air via mid-IR laser filamentation.

Light bullets [25, 26] are non-diffractive and non-dispersive optical pulses. Solids in the anomalous group-velocity dispersion (GVD) regime have been shown to support light bullets at 1.8 μm [27] and 1.9 μm [28], and light bullets have been predicted to propagate with the aid of resonant radiation [29]. Extending the concept to long wavelengths, Voronin *et al.* [30] predicted optical solitary wave propagation at 3.9 μm in YAG. However, light bullet propagation at even longer wavelengths, into the LWIR, has not been reported.

Recently, a lot of research efforts are also being undertaken for laser filamentation and nonlinear optics at long wavelengths in condensed matter [31]. For instance, mid-IR filamentation in solids has been shown to be effective for the probing of material band structure via HHG [31], supercontinuum generation and pulse compression [32–34], and even sub-cycle pulse generation via self-compression [30, 35, 36]. However, many uncertainties remain, in particular about filamentation in solids in the mid-IR/LWIR. For instance, how similar is mid-IR/LWIR filamentation in solids to that in gaseous media, and is the arrest of beam collapse no longer dominated by plasma, as was shown to be true in air [18]? Are light bullets supported in the LWIR? To answer these questions, a systematic study of wavelength-scaled laser filamentation in solids is imperative.

In this study, we present a numerical investigation of mid-IR and LWIR pulse evolution in novel propagation regimes in solids. In particular, we explore wavelength-scaled filamentation in highly-nonlinear ZnSe [37–39], which is significantly different from gases due to the importance of plasma. Pulse propagation is modeled with carrier-resolved unidirectional pulse propagation equations (UPPE) [40–42], revealing unique temporal and spectral characteristics including extreme self-steepening and optical shock, and multi-octave spanning supercontinuum generation. Most notably, we identify highly stable, sub-cycle LWIR light bullets, which are self-compressed via a combination of anomalous dispersion, self-steepening and plasma. Our LWIR light bullets critically depend on enhanced plasma defocusing and absorption, which is in sharp contrast to 4-μm air light bullets [18] and 1.9-μm light bullets in fused silica [29] stabilized via radiation loss. Because of this stable, self-steepened sub-cycle propagation, mid-IR/LWIR laser filamentation in solids can be an excellent tool for HHG [14, 15] and potentially isolating attosecond pulses.

We use carrier-resolved, radially symmetric UPPE [40–

---

[*] Corresponding author: bshim@binghamton.edu

42] to model pulse propagation in ZnSe for a total propagation distance of 1.5 cm at central wavelengths of $\lambda = 4$ μm (normal GVD, with GVD parameter $k_2 = 7.5\times10^{-28}$ s^2/cm) and $\lambda = 6$, 8 and 10 μm (anomalous GVD, with $k_2 = -1.36\times10^{-27}$, -5.2×10^{-27} and -1.2×10^{-26} s^2/cm, respectively). Zero GVD occurs in ZnSe at $\lambda \sim 4.8$ μm. ZnSe is chosen due to its high nonlinearity [37–39, 43] and broad transmission bandwidth in the mid-IR/LWIR. The input power is set to 7 times the critical power for self-focusing (P_{cr}) with $\lambda = 4$ μm, and $4P_{cr}$ with $\lambda =$ 6, 8, and 10 μm. These powers are low enough to avoid multifilamentation, which our radially-symmetric model cannot account for. The critical power in bulk media is defined as $P_{cr} = \frac{\alpha\lambda^2}{4\pi n n_2}$ [10], where n is the refractive index, n_2 is the nonlinear refractive index coefficient, and α is a factor that depends on the mode profile ($\alpha = 1.8962$ for a Gaussian beam). In our calculations $n_2 \sim 7\times10^{-15}$ cm^2/W, which has very little dispersion at the wavelengths used in ZnSe [43]. For $\lambda = 4$, 6, 8 and 10 μm, $P_{cr} \sim 1.4$, 3.2, 5.7 and 9 MW, respectively. For each wavelength, the full width at half-maximum (FWHM) input pulse duration is 60 fs and the input 1/e^2 beam radius is 100 μm.

The evolution of the electric field is described in the spectral domain with the UPPE as [40–42]:

$$\frac{\partial\widetilde{E}}{\partial z} = \frac{i}{2k(\omega)}\nabla_\perp^2\widetilde{E} + iD\widetilde{E} + \frac{i}{2k(\omega)}\frac{\omega^2}{c^2}\frac{\widetilde{P}_{NL}}{\epsilon_0} - \frac{1}{2k(\omega)}\frac{\omega}{c}\frac{\widetilde{J}}{\epsilon_0 c} - \frac{\widetilde{\alpha}_{NL}}{2} \tag{1}$$

We solve for the field $\widetilde{E}$ in Fourier space over the propagation distance, z. Here the wavevector is $k(\omega) = n(\omega)\omega/c$, where ω is the angular frequency, c is the speed of light, and $D = k(\omega) - \omega/v_g$, where v_g is the group velocity. $\widetilde{P}_{NL}$ is the Fourier transform of the nonlinear polarization in the time domain given by $P_{NL} = \epsilon_0\chi^{(3)}E^3$. Here ϵ_0 is the permittivity of free space and $\chi^{(3)}$ is the third-order nonlinear susceptibility. The free charge-induced current in the spectral domain is $\widetilde{J} = (e^2/m_e)(\nu_e + i\omega)/(\nu_e^2 + \omega^2)\widetilde{\rho E}$, where m_e and e are the electron mass and charge, respectively, ν_e is the electron collision frequency, and ρ is the free electron density. Absorption due to field ionization is accounted for by $\widetilde{\alpha}_{NL}$, which is the Fourier transform of $\alpha_{NL} = \frac{\rho_0 W(I) U}{I}E$, where ρ_0 is the neutral atomic density (2.2×10^{22} cm^{-3} in ZnSe), $W(I)$ is the field ionization rate, $U = 2.82$ eV is the band gap in ZnSe [44], and I is the intensity of the pulse. The right-hand side of Eq. (1) contains terms representing diffraction, dispersion, nonlinear polarization, plasma effects, and absorption due to field ionization, respectively.

UPPE are coupled to a plasma generation equation, which considers field ionization, collisional ionization and plasma recombination. The complete Keldysh optical field ionization rate in condensed matter is given by [45]:

$$W = \frac{2\omega_0}{9\pi}\Big(\frac{\omega_0 m^*}{\hbar\sqrt{\Gamma}}\Big)^{3/2} Q * exp(-\alpha\langle x+1\rangle)/\rho_0 \tag{2}$$

$$\Gamma = \frac{\gamma^2}{\gamma^2+1}, \qquad \Theta = \frac{1}{\gamma^2+1} \tag{3, 4}$$

$$Q = \sqrt{\frac{\pi}{2K(\Theta)}} \times \sum_{n=0}^{\infty} exp(-n\alpha)\varphi(\sqrt{\beta(2\nu+n)}) \tag{5}$$

$$\alpha = \pi\frac{K(\Gamma)-H(\Gamma)}{H(\Theta)}, \qquad \beta = \frac{\pi^2}{4K(\Theta)H(\Theta)} \tag{6, 7}$$

$$x = \frac{2UH(\Theta)}{\pi\hbar\omega_0\sqrt{\Gamma}}, \qquad \nu = \langle x+1\rangle - x \tag{8, 9}$$

Here the Keldysh adiabaticity parameter [45] is $\gamma = \frac{\omega_0}{eE}\sqrt{m^*U}$, where ω_0 is the central angular frequency of the laser pulse, e is the fundamental electric charge, E is the laser electric field, m^* is the reduced mass between an electron-hole pair ($0.19m_e$ in ZnSe [46], where m_e is the mass of an electron), and U is the band gap. The neutral atomic density is ρ_0, $\hbar$ is the reduced Planck constant, and $\langle . \rangle$ denotes the integer part. K and H are complete elliptic integrals of the first and second kinds, respectively, and φ is the Dawson function. In the regime of multiphoton ionization ($\gamma \gg 1$), Eq. (2) is simplified to the multiphoton ionization rate [3]:

$$W_{MPI} = \sigma_k I^k \tag{10}$$

Here k is the number of photons for multiphoton ionization, σ_k is the multiphoton ionization cross section, and I is the intensity of the laser pulse. In the tunneling ionization limit ($\gamma \ll 1$), Eq. (2) is expressed as [47]:

$$W_{TI} = \frac{4}{9\pi^2}\frac{U}{\hbar}\Big(\frac{m^*U}{\hbar^2}\Big)^{3/2}\Big(\frac{\hbar\omega}{U\gamma}\Big)^{5/2} \times exp\Big(-\frac{\pi U\gamma}{2\hbar\omega}(1-\frac{\gamma^2}{8})\Big)/\rho_0 \tag{11}$$

Plasma generation is described by [3]:

$$\frac{\partial\rho}{\partial t} = W(I)(\rho_0 - \rho) + \frac{\sigma_B I}{U}\rho - \frac{\rho}{\tau_r} \tag{12}$$

The first term on the right-hand side describes plasma generation due to optical field ionization, the second term describes collisional ionization, and the third term describes plasma recombination. Here ρ is the plasma density, $W(I)$ is the optical field ionization rate (either the full Keldysh optical field ionization rate, or the multiphoton or tunneling limit), σ_B is the inverse Bremsstrahlung cross section, and $\tau_r = 150$ fs is the plasma recombination time.

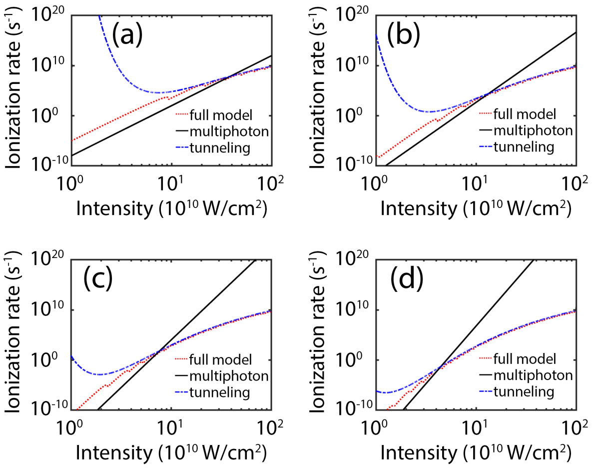

FIG. 1. (color online) Calculated optical field ionization rates are shown in each graph as a function of intensity for the full Keldysh optical field ionization rate (red dotted lines), the multiphoton ionization rate (black solid lines) and the tunneling ionization rate (blue dashed lines). Rates are shown for ZnSe at central wavelengths of (a) λ = 4, (b) λ = 6, (c) λ = 8, and (d) λ = 10 μm.

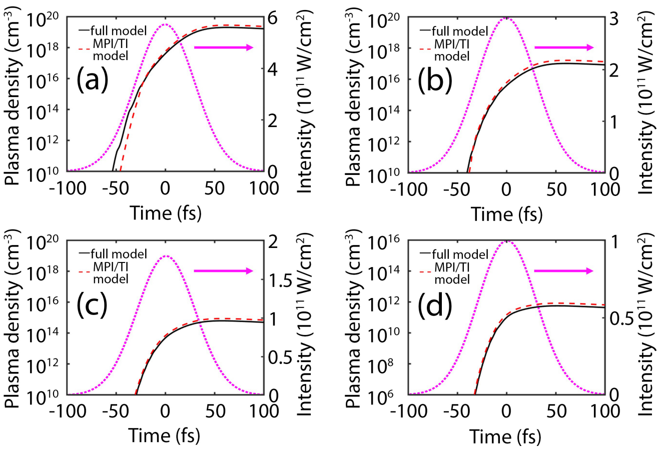

FIG. 2. (color online) Calculated plasma densities resulting from a laser pulse with a Gaussian temporal profile and a FWHM pulse duration of 60 fs in ZnSe. Plasma is generated due to both optical field ionization and collisional ionization. Plasma densities are calculated with the complete Keldysh ionization rate (labeled as black solid lines, full model) and with the multiphoton and tunneling ionization rates (labeled as red dashed lines, MPI/TI model). Input wavelengths λ and input peak intensities I_0 are (a) λ = 4, I_0 = 5.7×10^{11}, (b) λ = 6, I_0 = 3×10^{11}, (c) λ = 8, I_0 =1.8×10^{11}, and (d) λ = 10 μm, I_0 = 1×10^{11} W/cm^2. Laser intensity profiles are shown in magenta and labeled on the right vertical axis.

Equation (12) is incorporated into our UPPE model, where $W(I)$ is modeled with either multiphoton or tunneling ionization, depending on which rate more closely agrees with the complete Keldysh optical field ionization rate at a particular wavelength and peak intensity. By using either multiphoton or tunneling ionization, the UPPE calculation is significantly less computationally intensive than with the complete Keldysh model. For each wavelength, when the intensity is below a threshold intensity (where the multiphoton ionization rate equals the complete Keldysh ionization rate), the multiphoton rate is used for plasma density calculations, since the tunneling ionization rate is inaccurate at low intensities. When the intensity is above the threshold intensity, the tunneling ionization rate is used for plasma density calculations, since the multiphoton rate is inaccurate at high intensities. Figure 1 shows the full optical field ionization rate, the multiphoton ionization rate, and the tunneling ionization rate in ZnSe at central wavelengths of 4, 6, 8 and 10 μm, as a function of laser intensity. For λ = 4, 6, 8, and 10 μm, the threshold intensities are I_{th} = 3.4×10^{11}, 1.1×10^{11}, 6.8×10^{10}, and 4.1×10^{10} W/cm^2, respectively.

Figure 2 shows plasma generated by optical field ionization and collisional ionization, with a comparison between two cases of optical field ionization: the full model and the model that is used in our UPPE calculations, which switches between multiphoton ionization and tunneling ionization. Calculations are made for ZnSe at central wavelengths of λ = 4, 6, 8, and 10 μm, as a function of time in the presence of a laser pulse with a Gaussian temporal profile and a FWHM pulse duration of 60 fs. As shown in Fig. 2, there is excellent agreement between the full model and the model used for the UPPE calculations.

UPPE calculations yield peak intensities versus propagation distances that are shown in Fig. 3(a). Filaments reach peak intensities of ∼ 1.2×10^{12}, ∼ 1.2×10^{12}, ∼ 1.1×10^{12}, and ∼ 9.5×10^{11} W/cm^2 with λ = 4, 6, 8 and 10 μm, respectively. Generated peak plasma densities are ∼ 1×10^{19}, ∼ 2.1×10^{19}, ∼ 6.6×10^{18}, and ∼ 3.3×10^{18} cm^{-3} with λ = 4, 6, 8 and 10 μm, respectively, as shown in Fig. 3(b). These high plasma densities show that ionization effects are important during mid-IR/LWIR filamentation in solids. This is in sharp contrast to calculations of mid-IR/LWIR filamentation in gases [17, 48], where plasma densities decrease as the driver wavelength increases. Differences in ionization effects between gases and solids are particularly critical for light bullet generation, which will be highlighted later.

To understand the effects of energy loss during propagation, the energy of the pulse is calculated for each

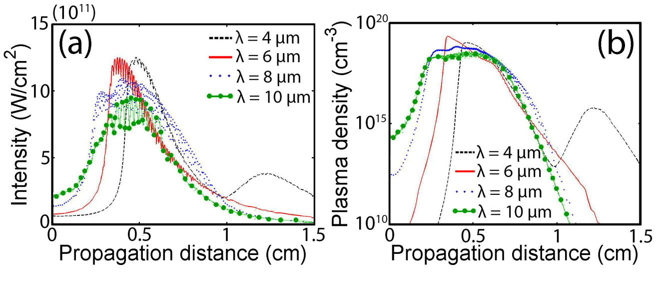

FIG. 3. (color online) Peak intensities and peak plasma densities versus propagation distance are shown in (a) and (b), respectively, for central wavelengths of λ = 4 (black dashed lines), λ = 6 (red solid lines), λ = 8 (blue dotted lines), and λ = 10 μm (green solid lines with circles).

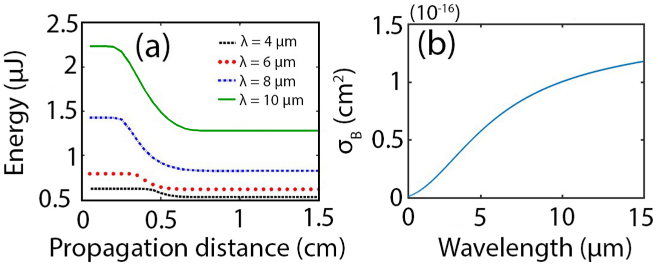

FIG. 4. (color online) Calculated energies in pulses at each wavelength during propagation are shown in (a), and the inverse Bremsstrahlung cross-section in ZnSe, σ_B, is shown in (b).

wavelength over the entire propagation distance by spatial and temporal integration of the spatio-temporal intensity profiles. Figure 4(a) shows the energies as a function of propagation distance. Energy losses with $\lambda = 4$, 6, 8, and 10 μm are 15%, 22%, 43% and 43%, respectively. These losses are mainly due to plasma generation and plasma absorption. Energy loss increases at longer wavelengths due to increased plasma absorption, which is described by the inverse Bremsstrahlung cross-section, σ_B (λ) [3], as shown in Fig. 4(b). Additionally, since stable filamentation occurs over longer distances with longer wavelengths (see Fig. 3), larger cumulative plasma densities are generated at long wavelengths, which further increases loss.

Supercontinuum generation leads to broadened spectra at all wavelengths, as shown by the spatially-averaged spectral profiles versus propagation distance in Fig. 5. On-axis spectral profiles at the input and at positions of shortest on-axis pulse durations are shown in Fig. 6: with $\lambda = 6$ and 8 μm [Figs. 6(b, c)], on-axis supercontinuum (via self-phase modulation [SPM]) at the 10^{-2} intensity level spans over 3 and over 2 octaves, respectively. Almost 2 octaves are spanned with $\lambda = 10$ μm [Fig. 6(d)], which is narrower than with $\lambda = 6$ and 8 μm due to lower intensities with $\lambda = 10$ μm [see Fig. 3]. Third-harmonic (TH) signals are visible for each wavelength during early propagation.

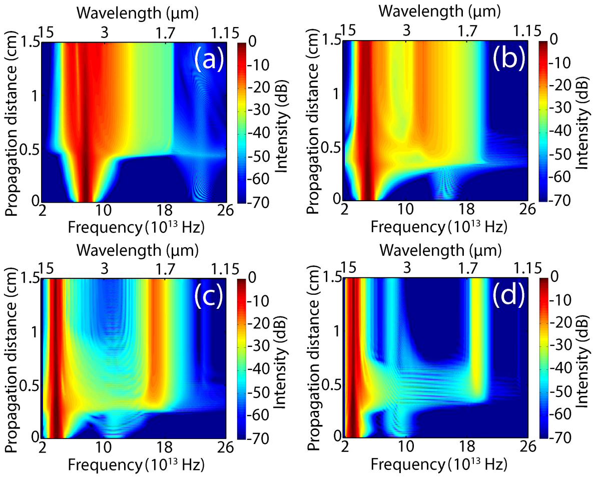

FIG. 5. (color online) Spatially-averaged spectral profiles versus propagation distance are shown for (a) $\lambda = 4$, (b) $\lambda = 6$, (c) $\lambda = 8$, and (d) $\lambda = 10$ μm. The color bars show spectral intensity in dB.

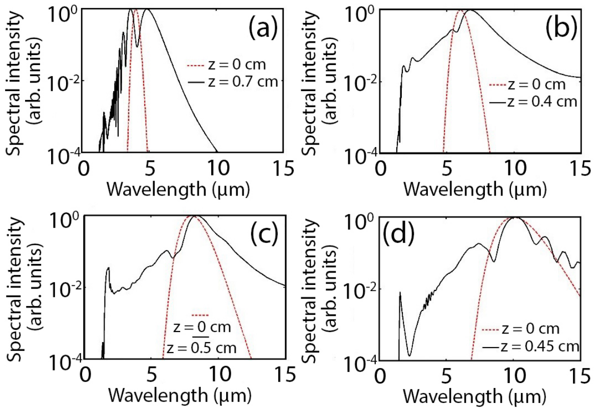

FIG. 6. (color online) Normalized on-axis spectral profiles at the input (red dashed lines) and at labeled positions of shortest on-axis pulse duration (black solid lines) are shown with (a) $\lambda = 4$, (b) $\lambda = 6$, (c) $\lambda = 8$, and (d) $\lambda = 10$ μm.

As shown by the spatio-temporal intensity profiles in Fig. 7, an extremely steep trailing edge forms during propagation, especially at 6 and 8 μm, which leads to optical shock, similar to that calculated previously in condensed matter [30, 49] and gases [17, 18, 20, 22, 49]. This steep trailing edge enhances the generation of high frequencies via SPM [3]. The temporal modulations shown in Fig. 7 and elsewhere in this work are due to the carrier resolution of the UPPE model. Intensity envelopes are retrieved for all figures with temporal modulations (see Appendix D for more details). Large plasma densities also contribute to the spectral blue shift.

According to our calculations, high-frequency peaks appear in the spatially-averaged (on-axis) spectra at 2.45 (2.5), 1.82 (1.85) and 1.57 (1.61) μm for central wavelengths of $\lambda = 6$, 8 and 10 μm, respectively. These peaks resemble those of resonant radiation (also known as dispersive waves, Cherenkov radiation and nonsolitonic radiation) shown in Fig. 1 of Brée *et al.* [29]. To investigate the possible role of resonant radiation in our calculations, we consider the phase-matching condition for resonant radiation, where the phase of the soliton $\varphi(\omega_s) = k(\omega_s)z - \omega_s \frac{z}{v_g} + \frac{\omega_s n_2 I_s z}{2c}$ matches that of the resonant radiation $\varphi(\omega) = k(\omega)z - \omega\frac{z}{v_g}$ [50]. Here ω_s is the angular frequency of the soliton, k is the wavenumber, z is the propagation distance, v_g is the group velocity of the soliton, n_2 is the nonlinear index coefficient, I_s is the intensity of the soliton, c is the speed of light, and ω is the angular frequency of the generated resonant radiation. Setting $\varphi(\omega_s) = \varphi(\omega)$, the phase-matching condition for resonant radiation can be expressed as:

$$\Delta k_{RR} = k(\omega) - k(\omega_s) + \frac{\omega_s - \omega}{v_g} - \frac{\omega_s n_2 I_s}{2c} \qquad (13)$$

Resonant radiation is expected to occur efficiently when $\Delta k_{RR} = 0$ rad/m. We solve Eq. (13) at propagation distances where self-focusing occurs, yielding eventual filamentation: $z = 0.32$, 0.22 and 0.186 cm with $\lambda = 6$, 8 and 10 μm, respectively. The quantities k and v_g, which depend on the material dispersion, are calculated using the plasma-dependent refractive index: $n(\omega) = [n_0(\omega)-1]\frac{(\rho_0-\rho)}{\rho_0}+1-\frac{\rho}{2\rho_c}$, where $n_0(\omega)$ is the refractive index in a neutral medium based on the Sellmeier equation, ρ is the plasma density, ρ_0 is the neutral medium density, and ρ_c is the critical plasma density. At the propagation distances considered, $\rho \sim 3.2\times10^{17}$, 2×10^{17} and 1×10^{17} cm^{-3}, and $I_s \sim 7\times10^{11}$, 5.9×10^{11}, and 3.7×10^{11} W/cm^2 with $\lambda = 6$, 8 and 10 μm, respectively. We also consider any shifts in the central wavelength of the soliton during propagation: $\lambda = 6$, 8 and 10 μm are shifted to 6.4, 8.2 and 10.1 μm, respectively, at the considered propagation distances.

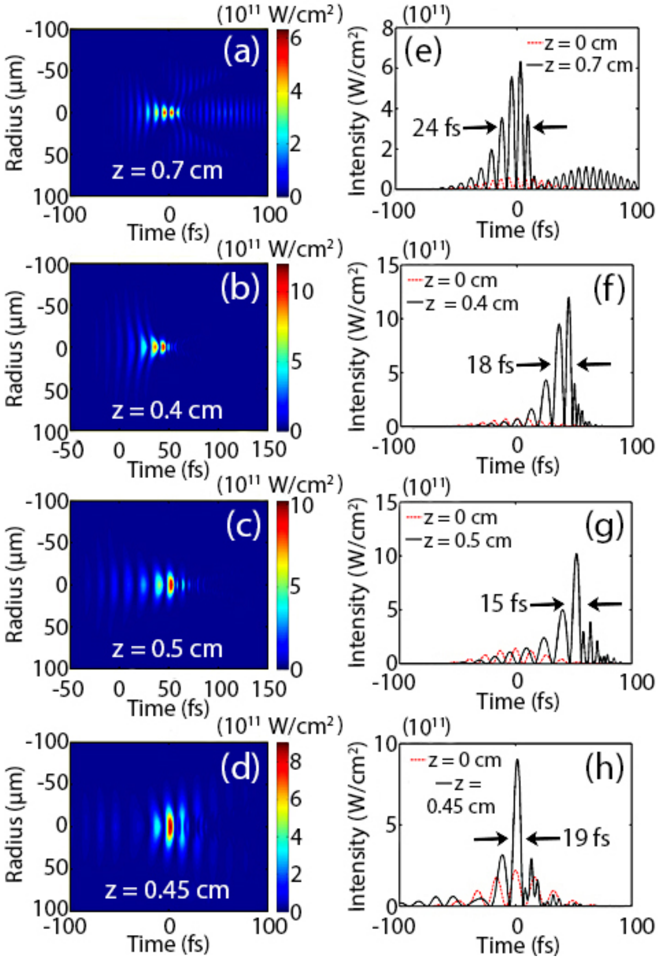

FIG. 7. (color online) Spatio-temporal intensity profiles at labeled propagation distances of shortest pulse duration are shown for (a) $\lambda = 4$, (b) $\lambda = 6$, (c) $\lambda = 8$, and (d) $\lambda = 10$ μm. The corresponding on-axis lineouts of the intensity profiles are shown for (e) $\lambda = 4$, (f) $\lambda = 6$, (g) $\lambda = 8$, and (h) $\lambda = 10$ μm, at the input (red dotted lines) and the position of shortest pulse duration (black solid lines). The color bars show intensity in W/cm^2, and on-axis pulse durations are labeled with arrows.

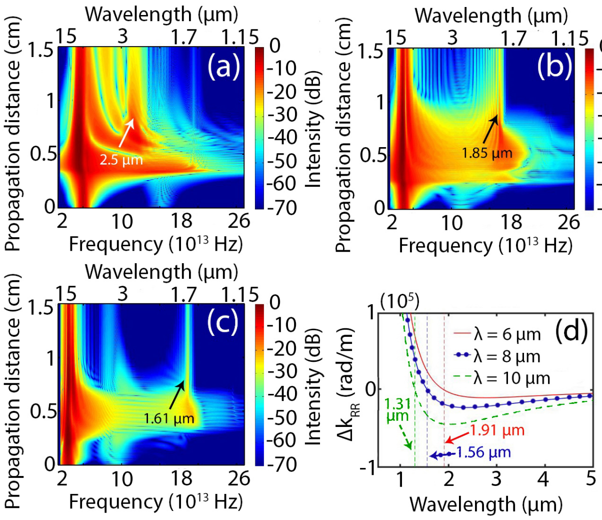

FIG. 8. (color online) On-axis spectral profiles versus propagation distance are shown for (a) $\lambda = 6$, (b) $\lambda = 8$, and (c) $\lambda = 10$ μm. The color bars show spectral intensity in dB, and arrows point to high-frequency components that may be due to resonant radiation. Phase-matching calculations for resonant radiation are shown in (d) for $\lambda = 6$ μm (red solid lines), $\lambda = 8$ μm (blue solid lines with circles) and $\lambda = 10$ μm (green dashed lines). Dashed vertical lines with colors matching fundamental wavelengths are shown for wavelengths that are phase-matched for resonant radiation ($\Delta k_{RR} = 0$ rad/m).

Phase-matching calculations for resonant radiation are shown in Fig. 8(d), which are compared with on-axis spectral profiles versus propagation distances in Fig. 8(a – c). As shown in Fig. 8(d), $\Delta k_{RR} = 0$ rad/m at resonant radiation wavelengths of 1.91, 1.56 and 1.31 μm for input wavelengths of $\lambda = 6$, 8 and 10 μm, respectively, in good agreement with our observations (the resonant radiation may be red-shifted by a few hundred nm at most to match the observed values of 2.5, 1.85 and 1.61 μm). The 2.5-μm signal with $\lambda = 6$ μm may also be due to third-harmonic generation. With $\lambda = 10$ μm, there is another prominent peak at ~ 3.65 μm, which is likely the red-shifted third harmonic of the fundamental beam.

On-axis spectra also exhibit additional high-frequency peaks that are not explained by the standard resonant radiation phase-matching in Eq. (13). For example, with $\lambda = 6$ μm, a peak at 1.53 μm is visible after $z \sim 0.75$ cm. This peak may be due to a mechanism based on the coupling of the fundamental pulse to the negative-frequency branch of the dispersion relation, known as negative-frequency resonant radiation [51], where phase-matching is described by:

$$\Delta k_{NRR} = k(\omega) - k(\omega_s) + \frac{\omega_s - \omega}{v_g} + 2\Big(\frac{n(\omega_s)\omega_s}{c} - \frac{\omega_s}{v_g}\Big) + \frac{\omega_s n_2 I_s}{2c} \qquad (14)$$

Using this phase-matching condition, calculations show that negative-frequency resonant radiation is phase-matched at 1.33 μm for the $\lambda = 6$-μm beam at $z = 0.32$ cm, which is close to the observed value of 1.53 μm. As we will show later, although resonant radiation is observed in our calculations, it is not the dominant mechanism for light bullet formation, in contrast to the 1.9-μm light bullet generated by resonant radiation in Ref. [29]. In the LWIR, the primary collapse-arresting/light bullet generation mechanism is enhanced plasma absorption and defocusing. This is also consistent with the calculation in Ref. [29] in which a longer wavelength shows less effects of resonant radiation (2 μm vs. 1.9 μm).

Self-compression occurs with all central wavelengths, as shown by the calculated on-axis temporal profiles versus propagation distance in Fig. 9. Anomalous GVD, SPM, plasma, and extreme self-steepening (shown in spatio-temporal intensity profiles in Fig. 7) yield on-axis FWHM pulse durations of $\sim$ 18, $\sim$ 15, and $\sim$ 19 fs for $\lambda = 6$, 8, and 10 μm, each below single cycle durations of 20, 27, and 33 fs, respectively. At $\lambda = 4$ μm, on-axis pulse durations are compressed to $\sim$ 24 fs, which is due to plasma and self-steepening. Sub-cycle on-axis pulse durations persist over many dispersion lengths (L_{ds}) during filamentation ($\sim 25L_{ds}$ and $\sim 23L_{ds}$ for $\lambda = 8$ and 10 μm, respectively). Spatially-averaged (over 35 μm) pulse durations versus propagation distance, shown in Fig. 10(a), reveal that for central wavelengths of $\lambda = 8$ and 10 μm, beams propagate as sub-cycle temporal solitary waves for many dispersion lengths. For example, with $\lambda = 8$ μm, the FWHM pulse duration is bounded between 24 and 26 fs over propagation from $z = 0.4$ cm to at least 0.6 cm, which is over 4 times the dispersion length [L_{ds}(26 fs) < 0.05 cm]. At $\lambda = 10$ μm, temporal solitary waves persist for over 10 times the dispersion length, with a pulse duration between 25 fs and 29 fs. With $\lambda = 4$ and 6 μm, temporal solitary waves are not observed.

It is important to compare the sub-cycle self-compression mechanism occurring here with previous studies. The mechanism of compression in ZnSe at mid-IR/LWIR wavelengths is similar to that observed previously in fused-silica at 1.9 μm [27], giving rise to light bullets [26]: SPM generates low frequencies near the leading edge of the pulse, and they are swept towards the trailing edge in anomalous dispersion. High frequencies are generated near the trailing edge, and are swept forward. Since high-density plasma is generated in ZnSe, plasma defocusing, which is mainly responsible for pulse compression in noble gases [52, 53], should contribute to light bullet generation. Moreover, Refs. [53] and [54] reported that self-steepening can assist in further compression. However, in noble gases dispersion plays a very small role in compression. The compression which occurs in normal dispersion in the present work is mainly plasma-assisted, but does not result in sub-cycle pulse durations. This is in contrast to the sub-cycle pulse compression occurring in anomalous dispersion, which shows the important role of dispersion for sub-cycle compression in solids. We will show later that dispersion effects in ZnSe are assisted by plasma, yielding favorable conditions for light bullet generation by extending the anomalous dispersion bandwidth. This is also in contrast to recently reported light bullet generation in air at 4 μm [18], where dynamics are influenced strongly by radiation loss rather than plasma/defocusing loss. Similarly, plasma effects were shown to be negligible during propagation in gases at 2 μm where dynamics during compression were strongly influenced by initial carrier-envelope phase and harmonic generation [54]. Other notable mechanisms for self-compression have been proposed in solids, such as efficient spectral broadening via cascaded four-wave mixing during propagation in GaAs near zero GVD [35]. However, in ZnSe zero GVD occurs near $\sim$ 4.8 μm, and efficient compression occurs even with $\lambda = 10$ μm, so the mechanism proposed in Ref. [35] is quite different from that in our work.

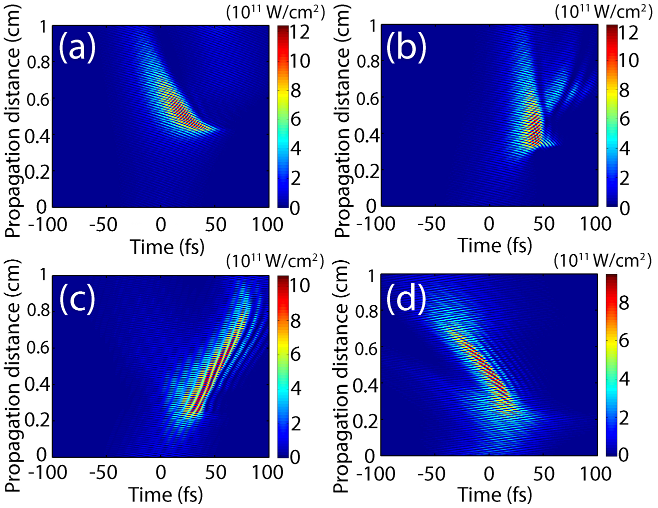

FIG. 9. (color online) On-axis temporal profiles versus propagation distance are shown for (a) $\lambda = 4$, (b) $\lambda = 6$, (c) $\lambda = 8$, and (d) $\lambda = 10$ μm. The color bars show intensity in W/cm^2.

Strikingly, sub-cycle light bullets [25, 26] propagate with $\lambda = 8$ μm. The temporally-averaged beam diameter [Fig. 10(b)] during filamentation is $\sim$ 28 μm, with minimal change. This results in light bullet propagation from $z = 0.4$ cm to at least $z = 0.6$ cm, which is a propagation distance of $\sim 4.2L_{ds}$ and $\sim$3.6L_{df} at a FWHM pulse duration of $\sim$ 26 fs (see examples of spatio-temporal intensity profiles in Fig. 11). In particular, the light bullet propagates stably as a self-steepened waveform at sub-cycle pulse durations with a dominating (most intense) cycle, providing a robust and promising tool for potential attosecond pulse isolation and HHG [14, 15]. For instance, Chin *et al.* [55] measured up to the 7th harmonic from ZnSe using 3.9-μm, 200-fs beams at an intensity $\sim 10^{11}$ W/cm^2. Since our peak intensity is one order of magnitude larger with a longer harmonic driver wavelength and sub-cycle pulse duration, we expect that higher-order harmonics should be generated. Furthermore, we believe our method can be applied to HHG from any bulk crystals in which long-wavelength laser

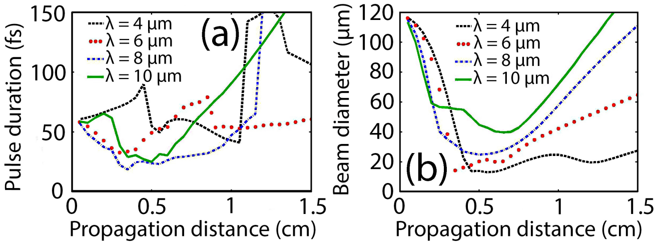

FIG. 10. (color online) Spatially-averaged FWHM pulse durations (a) and temporally-averaged FWHM beam diameters (b) versus propagation distance for $\lambda = 4$ (black dashed lines), $\lambda = 6$ (red circles), $\lambda = 8$ (blue dot-dash lines), and $\lambda = 10$ μm (green solid lines).

pulses undergo filamentation and pulse compression in the anomalous-GVD regime. We also check propagation with $\lambda = 8$ μm for different powers and a different input pulse duration (see Appendix A for more details). Light bullets still propagate at higher input powers, but they are not observed with longer input pulse durations. Compared to temporal solitons in fibers, our light bullets have soliton numbers that do not exceed 1.4 and are thus similar to fundamental solitons [56].

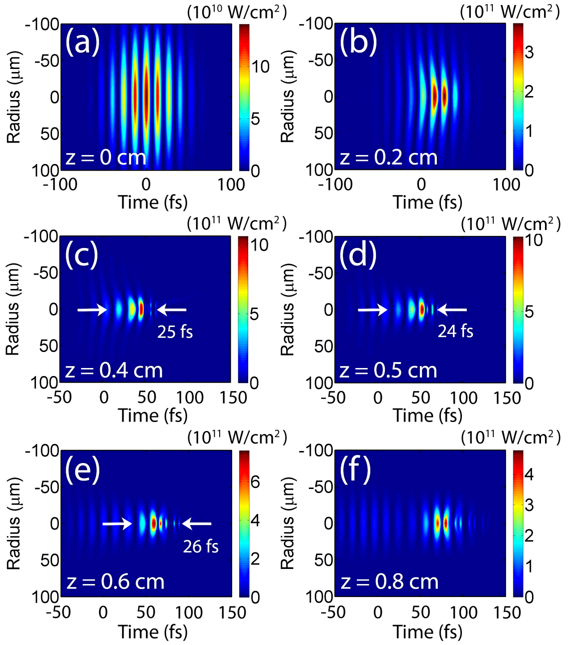

FIG. 11. (color online) Spatio-temporal intensity profiles are shown for $\lambda = 8$ μm at (a) $z = 0$, (b) $z = 0.2$, (c) $z = 0.4$, (d) $z = 0.5$, (e) $z = 0.6$, and (f) $z = 0.8$ cm. A light bullet persists from $z = 0.4$ to $z = 0.6$ cm. The color bars show intensity in W/cm^2, and spatially-averaged pulse durations are labeled with arrows where light bullets propagate.

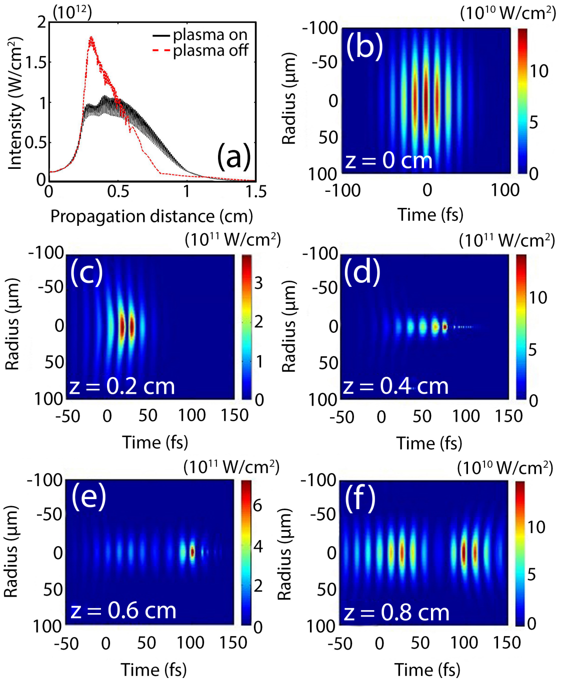

FIG. 12. (color online) Peak intensity versus propagation distance with $\lambda = 8$ μm is shown in (a) without plasma (red dashed lines) and with plasma (black solid lines). Spatio-temporal intensity profiles without plasma are shown at (b) $z = 0$, (c) $z = 0.2$, (d) $z = 0.4$, (e) $z = 0.6$ cm and (f) $z = 0.8$ cm. The color bars show intensity in W/cm^2.

In contrast to the negligible effects of plasma in gases at similar central wavelengths [18], ionization effects here significantly impact filamentation and light bullet generation. For example, in Ref. [18] a plasma density of $\rho \sim 7{\times}10^{14}$ cm^{-3} with $\lambda = 4$ μm yields an index contribution due to plasma ($n_p \propto -\frac{\rho}{2\rho_c}$, where ρ_c is the critical plasma density) of $n_p \sim -5{\times}10^{-6}$ compared to a neutral index of ~ 1, whereas in ZnSe at 4 μm, with a plasma density of $\rho \sim 1{\times}10^{19}$ cm^{-3} (based on our calculations), $n_p \sim -0.07$, compared to a neutral index of ~ 2.4. Therefore, the effects of plasma are significantly greater in solids. Note that in Ref. [49] small plasma densities are generated during carrier-shock formation at 8 μm in single-crystal diamond. However, this is mainly due to diamond's high ionization energy (5.5 eV), yielding low plasma densities.

To investigate the effects of plasma on the filamentation dynamics, calculations are performed with $\lambda = 8$ μm and an input power of $4P_{cr}$, but plasma generation is turned off. For these calculations, terms describing field ionization, collisional ionization, and plasma absorption are set to zero. The FWHM pulse duration is set to 60 fs and the input 1/e^2 beam radius is set to 100 μm. In contrast to air, where the effects of plasma are small [18], the resulting spatio-temporal dynamics in ZnSe without plasma are drastically different. Without plasma in our calculations, an abrupt intensity spike occurs during early propagation (around $z = 0.35$ cm), as shown in Fig. 12(a), which shows the importance of plasma as a mechanism for arresting collapse and formation of a stable filament and light bullet. Spatio-temporal intensity profiles [Fig. 12(b − f)] reveal that self-steepening still occurs without plasma, but the pulse abruptly splits into two portions of lower peak intensities, preventing collapse [Fig. 12(f)]. Neither temporal nor spatial solitary wave behavior is observed over extended propagation distances

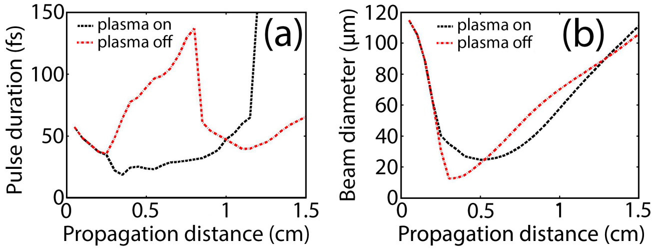

FIG. 13. (color online) Spatially-averaged FWHM pulse durations (a) and temporally-averaged FWHM beam diameters (b) are shown with plasma (black dashed lines) and without plasma (red dot-dashed lines). Calculations are performed with $\lambda = 8$ μm and an input power of $4P_{cr}$.

without plasma, as shown in Fig. 13(a) (pulse duration) and Fig. 13(b) (beam diameter).

Spatially-averaged spectral profiles comparing the cases with plasma [Fig. 14(a)] and without plasma Fig. 14(b)] reveal that for the case without plasma, the pulse contains significantly less high-frequency content over the entire propagation distance ($\sim$ 1 order of magnitude lower spectral intensity than with plasma at spectral components with $\lambda < 2$ μm by the end of propagation). This is due to the spectral blue shift associated with plasma [3], which provides high-frequency components during propagation.

GVD parameters are calculated using the frequency- and plasma-dependent refractive index, defined as $n(\omega)$ $= [n_0(\omega) - 1]\frac{(\rho_0 - \rho)}{\rho_0} + 1 - \frac{\rho}{2\rho_c}$, where $n_0(\omega)$ is the refractive index in a neutral medium based on the Sellmeier equation, ρ_0 is the neutral medium density, ρ is the plasma density, ω is the angular frequency of the pulse, and ρ_c is the critical plasma density. Figure 15 shows calculated refractive indices and group velocity dispersion both with and without plasma. Furthermore, as shown in Figs. 15(b) and (c), the zero GVD wavelength is $\sim$ 4.8 μm without plasma, and with a plasma density of $\rho \sim 6\times10^{18}$ cm^{-3} it is shifted to $\sim$ 3.2 μm. This results in a significantly larger bandwidth for the anomalous-GVD regime with plasma, which can support pulse compression and light bullet propagation better.

We also perform cross-correlation frequency-resolved optical gating (XFROG) [57] with and without plasma to visualize the spectral content of the 8-μm propagation at different temporal positions. Furthermore, additional calculations show that the high plasma densities and non-monotonic wavelength scaling of plasma density in ZnSe (see Fig. 3) are due to high-frequency bursts at the pulses' trailing edge caused by high intensities and self-steepening, which is the result of propagation in the anomalous-GVD regime in a high-density solid. Details of the XFROG analysis and propagation at lower medium densities can be found in Appendices B and C, respectively.

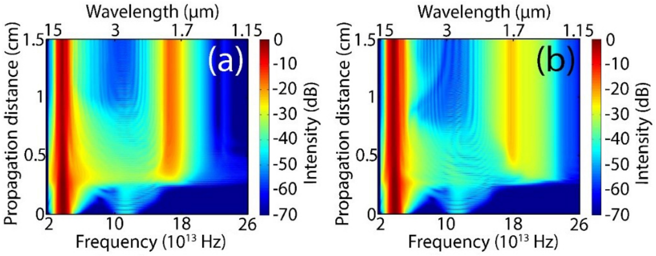

FIG. 14. (color online) Spatially-averaged spectral profiles versus propagation distance are shown with $\lambda = 8$ μm and an input power of $4P_{cr}$ with plasma (a) and without plasma (b). The color bars show spectral intensity in dB.

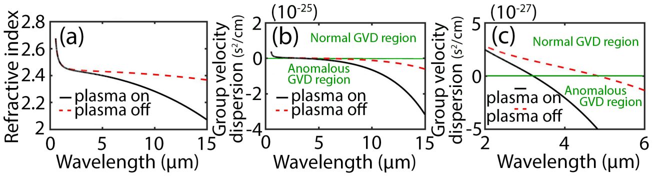

FIG. 15. (color online) Calculations of (a) refractive index, (b) GVD parameter and (c) GVD parameter zoomed in near zero GVD are shown with a plasma density of $\rho \sim 6\times10^{18}$ cm^{-3} (black solid lines) and without plasma (red dashed lines). In (b) and (c), the normal-GVD regime appears above the green horizontal line (GVD parameter > 0) and the anomalous-GVD regime appears below (GVD parameter < 0).

In conclusion, we have investigated the mid-IR/LWIR wavelength scaling of laser filamentation in ZnSe by solving carrier-resolved unidirectional pulse propagation equations. Our calculations reveal rich spatio-temporal dynamics, with extreme self-steepening leading to optical shock and multi-octave spanning supercontinuum generation at long central wavelengths. It is shown that unlike mid-IR/LWIR filamentation in gases, plasma in solids is important for stabilizing laser filamentation over an extended range and enhancing compressibility via extending a bandwidth of the anomalous-GVD regime. Furthermore, we predict the propagation of sub-cycle light bullets at $\lambda = 8$ μm for about 3.6 times the diffraction length and 4.2 times the dispersion length. These subcycle light bullets at LWIR can provide a promising tool for extreme nonlinear optics at long wavelengths including HHG and potential generation of attosecond pulses in solids.

This work is supported by National Science Foundation (NSF) (PHY-1707237) and Air Force Office of Scientific Research (AFOSR)(FA9950-18-1-0223).

APPENDIX A: SPATIO-TEMPORAL DYNAMICS WITH DIFFERENT INPUT PARAMETERS

To supplement our observation of light bullets at $\lambda = 8$ μm with an input power of $4P_{cr}$ (see main calculations for more details), we investigate filamentation in ZnSe with $\lambda = 8$ μm at input powers of $6P_{cr}$ and $8P_{cr}$ with input FWHM pulse durations of $\tau_p = 60$ fs and input

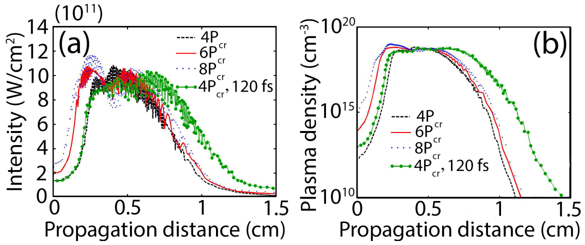

FIG. 16. (color online) Peak intensities and peak plasma densities versus propagation distance are shown in (a) and (b), respectively, with $\lambda = 8$ μm and input powers and input pulse durations of $4P_{cr}$, 60 fs (black dashed lines), $6P_{cr}$, 60 fs (red solid lines), $8P_{cr}$, 60 fs (blue dotted lines), and $4P_{cr}$, 120 fs (green solid lines with circles).

1/e^2 beam radii of 100 μm. Calculations are also performed for $\lambda = 8$ μm at $4P_{cr}$ with an input FWHM pulse duration of 120 fs and an input 1/e^2 beam radius of 100 μm. Figure 16 shows the peak intensity and peak plasma density versus propagation distance for the various input powers, including a reproduction of results shown in the main manuscript with $4P_{cr}$ and $\tau_p = 60$ fs. Filaments form with $6P_{cr}$, $8P_{cr}$ ($\tau_p = 60$ fs) and $4P_{cr}$ ($\tau_p = 120$ fs) over a similar range as $4P_{cr}$ ($\tau_p = 60$ fs) at a clamped peak intensity of $\sim 1.1{\times}10^{12}$ W/cm^2 and with peak plasma densities of $\sim 7.7{\times}10^{18}$ cm^{-3}.

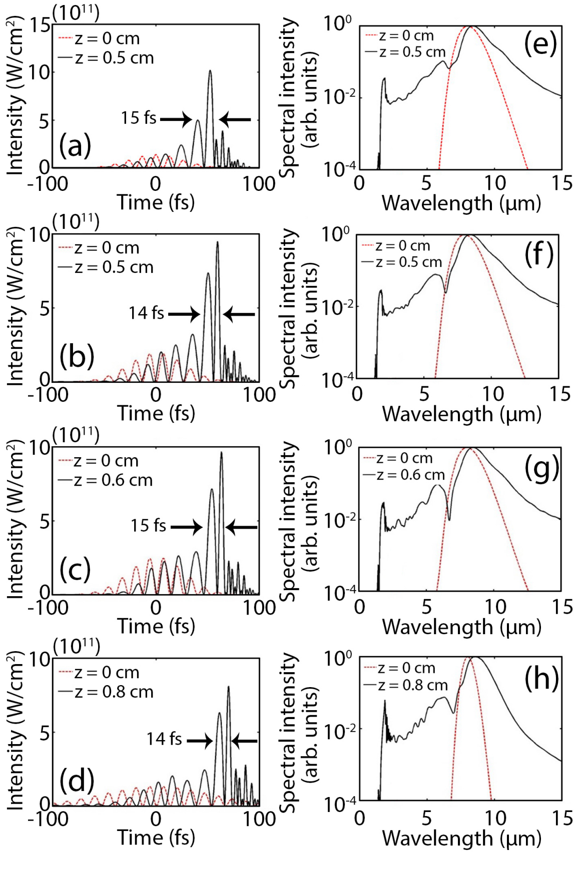

FIG. 17. (color online) On-axis temporal profiles (left column) and spectral profiles (right column) are shown at the input and at propagation distances where the pulse duration is minimized, as labeled. For each calculation, $\lambda = 8$ μm and input powers and input pulse durations are (a, e) $4P_{cr}$, 60 fs, (b, f) $6P_{cr}$, 60 fs, (c, g) $8P_{cr}$, 60 fs, and (d, h) $4P_{cr}$, 120 fs. On-axis pulse durations are labeled with arrows.

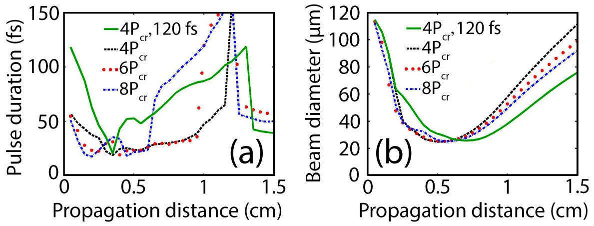

FIG. 18. (color online) Spatially-averaged FWHM pulse durations (a) and temporally-averaged FWHM beam diameters (b) versus propagation distance are shown at $\lambda = 8$ μm and input powers and input FWHM pulse durations of $4P_{cr}$, 120 fs (green solid lines), $4P_{cr}$, 60 fs (black dashed lines), $6P_{cr}$, 60 fs (red closed circles), and $8P_{cr}$, 60 fs (blue dot-dashed lines).

Figure 17 shows on-axis temporal and spectral profiles at the input and at positions of shortest pulse duration. Supercontinuum is generated over 2 octaves (at the 10^{-2} intensity level) with $6P_{cr}$ and $8P_{cr}$ ($\tau_p = 60$ fs) [Figs. 17(f) and (g), respectively], similar to that discussed in the main manuscript at $4P_{cr}$ ($\tau_p = 60$ fs) [reproduced here in Fig. 17(e)]. The spectrum is broadened by slightly under 2 octaves with $4P_{cr}$ ($\tau_p = 120$ fs) [Fig. 17(h)]. Self-steepening, anomalous GVD, and plasma result in sub-cycle pulse compression for each in-

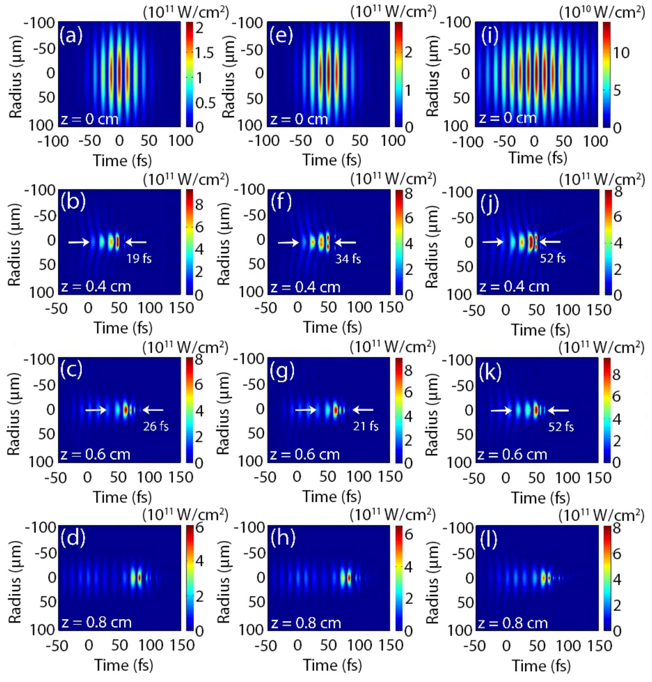

FIG. 19. (color online) Spatio-temporal intensity profiles are shown for $\lambda = 8$ μm at labeled propagation distances with input powers and input FWHM pulse durations of (a − d) $6P_{cr}$, 60 fs, (e − h) $8P_{cr}$, 60 fs, and (i − l) $4P_{cr}$, 120 fs. The color bars show intensity in W/cm^2, and selected spatially-averaged pulse durations are labeled with arrows.

put power and pulse duration [Figs. 17(a − d)]. Furthermore, with $6P_{cr}$ and $8P_{cr}$ ($\tau_p = 60$ fs), light bullet propagation at sub-cycle spatially-averaged (within the filamentation region of ~ 35 μm FWHM) pulse durations (18 − 23 fs) and temporally-averaged FWHM diameters (25 − 26 μm) is observed for distances of ~ 0.13 cm, corresponding to $\sim 3.5L_{ds}$ and $\sim 2.8L_{df}$ [Fig. 18], where L_{df} and L_{ds} are the diffraction length and dispersion length, respectively. Figure 19(a − h) shows spatio-temporal profiles of light bullets with input powers of $6P_{cr}$ and $8P_{cr}$ ($\tau_p = 60$ fs), which are similar to those with $4P_{cr}$ ($\tau_p = 60$ fs) (see main calculations). With a longer pulse duration, light bullets do not propagate. Spatio-temporal profiles are shown for this case in Fig. 19(i − l).

APPENDIX B: SPECTRAL CONTENT VISUALIZATION AT DIFFERENT TEMPORAL POSITIONS VIA XFROG

Without plasma, the beam splits temporally into pulses of similar intensity, preventing light bullet formation. When light bullets propagate with plasma, they are accompanied by low-intensity side lobes that propagate ahead and behind the main pulse. The main collapse-arresting mechanism with plasma is defocusing and absorption due to plasma, but energy leakage from the central solitary wave into the side lobes may assist prevention of collapse. Figure 20 shows on-axis intensity profiles from the main calculations ($\lambda = 8$ μm, $4P_{cr}$ input power), where a temporal solitary wave persists on axis from $z = 0.4$ to 0.8 cm. As shown in Fig. 20(d), extreme self-steepening at $z = 0.3$ cm produces a burst of high-frequency content that trails the central peak. Energy leakage into this high-frequency portion can aid the arrest of collapse, similar to that reported in air [18]. Furthermore, at $z = 0.4$ cm another lobe, which contains similar spectral content to the main pulse, begins to propagate ahead of the main pulse. This side lobe travels faster than the main peak, and the peak intensity of the lobe grows from 17% of the main self-steepened pulse at $z = 0.4$ cm to 50% by the end of propagation at $z = 1.5$ cm. Similar to the high-frequency content, this lobe may aid plasma defocusing/absorption in the arrest of collapse, as energy leaks from the main pulse into this lobe during propagation.

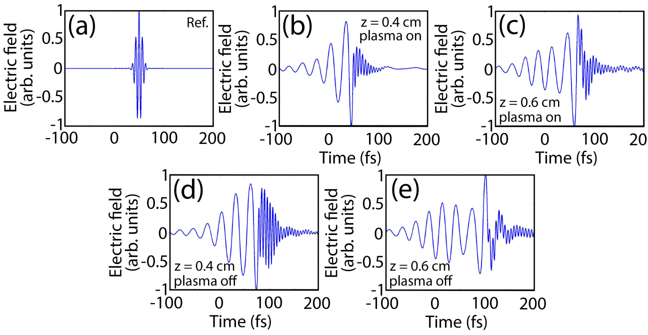

FIG. 21. (color online) Normalized on-axis electric fields are shown for (a) the XFROG reference (Ref.) pulse, (b) λ = 8-μm pulse, $z = 0.4$ cm, plasma on, (c) λ = 8-μm pulse, z = 0.6 cm, plasma on, (d) λ = 8-μm pulse, $z = 0.4$ cm, plasma off and (e) λ = 8-μm pulse, $z = 0.6$ cm, plasma off.

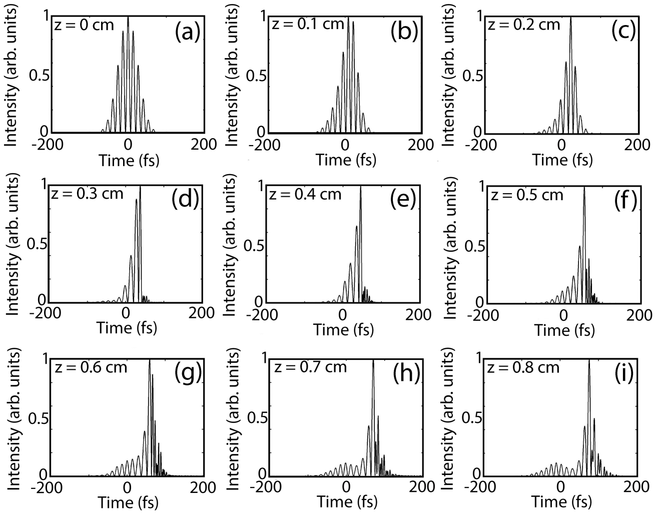

FIG. 20. Normalized on-axis intensity profiles are shown with $\lambda = 8$ μm and an input power of $4P_{cr}$ for various propagation distances as labeled: (a) $z = 0$, (b) $z = 0.1$, (c) $z = 0.2$, (d) $z = 0.3$, (e) $z = 0.4$, (f) $z = 0.5$, (g) $z = 0.6$, (h) $z = 0.7$, and (i) $z = 0.8$ cm.

To visualize the frequency content of the self-steepened

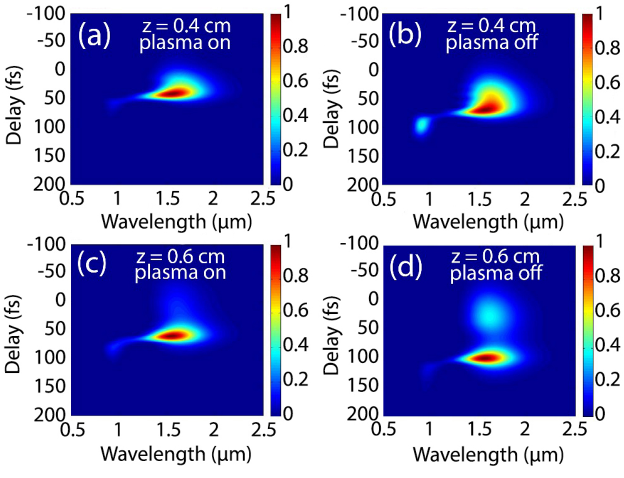

FIG. 22. (color online) XFROG spectrograms (normalized) are shown for the 8-μm beam with (a) plasma on, $z = 0.4$ cm, (b) plasma off, $z = 0.4$ cm, (c) plasma on, $z = 0.6$ cm, and (d) plasma off, $z = 0.6$ cm. Here the delay axis corresponds to the offset between the reference pulse and the signal pulse (to be analyzed), where a delay of 0 fs means the reference field at 0 fs is overlapped with the signal field at 0 fs (see examples of signal fields in Fig. 21). More positive delays show wavelength content at the trailing edge of the pulse.

main pulse and the side lobes in more detail, we perform cross-correlation frequency-resolved optical gating (XFROG) [57] on the $\lambda = 8$-μm beam on axis at $z = 0.4$ cm (light bullet propagation begins here) and $z = 0.6$ cm (light bullet propagation ends around here) both with plasma turned on and off. A reference pulse with a wavelength of $\lambda_{Ref} = 2$ μm and a FWHM pulse duration of 10 fs is used to measure sum frequency generation. Fig. 21 shows the reference pulse and the $\lambda = 8$-μm pulse electric fields to be characterized (normalized).

Figure 22 shows the XFROG spectrograms. For both with and without plasma, short wavelengths propagate at the trailing lobe (large positive delays in XFROG spectrogram), accompanied by a much smaller signal at long wavelengths. At $z = 0.4$ cm without plasma, where a large burst of high-frequency content occurs, the short-wavelength signal is much more intense than the long-wavelength signal at the trailing lobe [Fig. 22(b)]. The main pulse and the leading lobe are composed of broad bandwidths of long wavelengths, as can be seen in Fig. 22(c) and (d). Furthermore, the high-magnitude leading lobe at $z = 0.6$ cm without plasma indicates the onset of pulse splitting without plasma, preventing light bullets.

APPENDIX C: NON-MONOTONIC PLASMA-WAVELENGTH SCALING AND PROPAGATION WITH DIFFERENT MEDIUM DENSITIES

In the main calculations, the peak plasma densities are $\rho = 1\times10^{19}$, 2.1×10^{19}, 6.6×10^{18}, and 3.3×10^{18} cm^{-3} for $\lambda = 4$, 6, 8 and 10 μm, respectively. This result is quite different from gases because in gases peak plasma density decreases monotonically with increasing wavelength (for example, see Fig. 3(c) in [48] and Fig. 3(b) in [17]). As will be discussed, this is due to stronger high-frequency generation at $\lambda = 6$ μm because of high densities in solids. Figure 23 shows on-axis intensity profiles and on-axis plasma density growth at propagation positions where maximum plasma density is generated for each wavelength. Comparing profiles with $\lambda = 4$ μm at $z = 0.45$ cm [Figure 23(a, e)] to $\lambda = 6$ μm at $z = 0.35$ cm [Figure 23(b, f)], it is clear that with $\lambda = 6$ μm, more pronounced high-frequency bursts occur at the back of the pulse than the case with $\lambda = 4$ μm. High frequencies are also emitted with $\lambda = 4$, 8, and 10 μm, but the peak amplitude of these spectral components is not as high as with 6 μm. This efficient high-frequency generation with $\lambda = 6$ μm is mainly due to a combination of a high peak intensity ($I_0 = 1.2\times10^{12}$ W/cm^2 for $\lambda = 6$ μm compared to $I_0 = 1.1\times10^{12}$ and 9.5×10^{11} W/cm^2 with $\lambda = 8$ and 10 μm, respectively) and pronounced self-steepening (maximum $|\frac{dI}{dt}|$ over the entire propagation distance at the trailing edge is 2.17×10^{26} W/cm^2/s with $\lambda = 6$ μm compared to 1.47×10^{26} W/cm^2/s with $\lambda = 4$ μm). With $\lambda = 6$ μm, high frequencies are also made by third-harmonic generation, and/or by phase-matched resonant radiation, as discussed in the main manuscript.

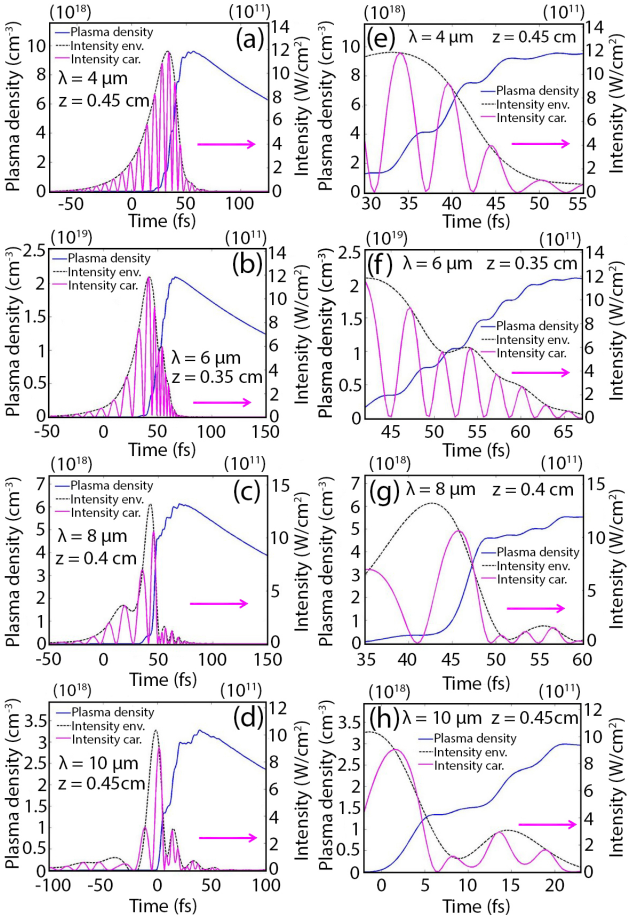

FIG. 23. (color online) On-axis intensity profiles (carrier in magenta [light gray] solid lines and envelope in black dotted lines) and on-axis plasma density (blue [dark gray] solid lines) are shown at labeled propagation distances of maximum plasma density with (a, e) $\lambda = 4$ μm, $z = 0.45$ cm (b, f) $\lambda = 6$ μm, $z = 0.35$ cm (c, g) $\lambda = 8$ μm, $z = 0.4$ cm and (d, h) $\lambda = 10$ μm, $z = 0.45$ cm.

To quantitatively extract the dominant frequency versus time for each pulse in the main calculations, we calculate the instantaneous frequency, $\omega_{inst} = -\frac{d\varphi}{dt}$, where φ is the temporal phase. Electric field profiles at propagation distances of maximum plasma density are shown in Fig. 24(a), (d), (g) and (j) for $\lambda = 4$, 6, 8 and 10 μm, and the temporal phase of each is shown in Fig. 24(b), (e), (h) and (k), respectively. According to our calculations, high-frequency components are especially pronounced for the 6-μm pulse. For example, at the temporal FWHM intensity position at the trailing edge of the 6-μm pulse (delay = 49 fs), the peak wavelength is ~ 2 μm. With the 4-μm pulse, at the temporal FWHM position at the trailing edge (delay = 42 fs), the peak wavelength is ~ 2.9 μm. Therefore, even though the input wavelength is 6 μm, extreme spectral broadening due to propagation in the anomalous-GVD regime yields frequencies that are higher than those generated by the 4-μm pulse. This high-frequency content propagating with the 6-μm pulse

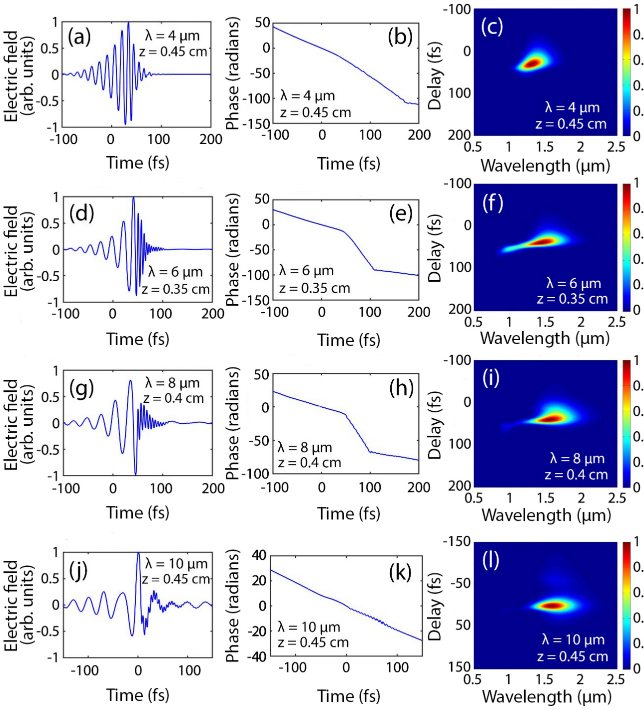

FIG. 24. (color online) On-axis normalized electric field temporal profiles are shown at labeled propagation distances of maximum plasma density with central wavelengths of (a) $\lambda = 4$, (d) $\lambda = 6$, (g) $\lambda = 8$ and (j) $\lambda = 10$ μm. The temporal phase of each field is shown for each central wavelength in (b) $\lambda = 4$, (e) $\lambda = 6$, (h) $\lambda = 8$ and (k) $\lambda = 10$ μm. Corresponding XFROG spectrograms (normalized) are shown for central wavelengths of (c) $\lambda = 4$, (f) $\lambda = 6$, (i) $\lambda = 8$ and (l) $\lambda = 10$ μm. Here the delay axis corresponds to the offset between the reference pulse and the signal pulse (to be analyzed), where a delay of 0 fs means the reference field at 0 fs is overlapped with the signal field at 0 fs. More positive delays show wavelength content at the trailing edge of the pulse.

is also a consequence of phase-matched resonant radiation (as discussed in the main manuscript). Furthermore, since these frequencies are generated at the back of the pulse, their interaction with plasma is an especially important factor that determines the peak plasma density, because the trailing edge is exposed to highest plasma densities. This high-frequency burst drastically alters the relative effects of plasma between the two central-wavelength calculations, which yields the non-monotonic scaling of plasma density versus wavelength. For instance, assuming the same plasma density ρ for both the $\lambda = 4$ and 6-μm pulses and considering the peak wavelengths at the trailing edge of each pulse (2.9 and 2.0 μm, respectively), the ratio of the refractive index change due to plasma $\Delta n_p \sim -\frac{\rho}{2\rho_c}$ (here $\rho_c \propto 1/\lambda^2$ is the critical plasma density) experienced by the trailing edges is $(\frac{\Delta n_{2.9\mu m}}{\Delta n_{2.0\mu m}} \sim 2.1$, whereas if the central wavelengths were unchanged, $\frac{\Delta n_{4\mu m}}{\Delta n_{6\mu m}} \sim 0.44$, which changes the plasma interaction significantly.

$\alpha = 1$			
$\lambda(\mu\text{m})$	$\tau_p(\text{fs})$	$w_0(\mu\text{m})$	$z_{total}(\text{cm})$
4	60	100	1.5
6	60	100	1.5
8	60	100	1.5
10	60	100	1.5
$\alpha = 0.5$			
$\lambda(\mu\text{m})$	$\tau_p(\text{fs})$	$w_0(\mu\text{m})$	$z_{total}(\text{cm})$
4	175	175	10
6	175	200	10
8	175	225	10
10	175	250	10
$\alpha = 0.1$			
$\lambda(\mu\text{m})$	$\tau_p(\text{fs})$	$w_0(\mu\text{m})$	$z_{total}(\text{cm})$
4	200	450	10
6	200	500	10
8	200	550	10
10	200	600	10
$\alpha = 0.05$			
$\lambda(\mu\text{m})$	$\tau_p(\text{fs})$	$w_0(\mu\text{m})$	$z_{total}(\text{cm})$
4	225	825	20
6	225	875	20
8	225	950	20
10	225	1000	20

TABLE I. Shown here are changes to parameters made in calculations at lower molecular densities. The quantities λ, τ_p, w_0 and z_{total} are the central wavelength, input pulse duration, input beam waist, and total propagation distance for each calculation. α is the fractional density coefficient used in each case.

The physical origin of this anomalous wavelength-scaled filamentation in solids is high densities in solids. In our additional simulations, we vary the neutral molecular density ρ_0 which is reduced to a fractional density $\alpha\rho_0$, where α is the fractional density coefficient set to 1, 0.5, 0.1, and 0.05 ($\alpha = 1$ gives the same results as the main calculations). This procedure is analogous to studying propagation in gases at different pressures, so we scale all parameters such as dispersion, linear and nonlinear indices, collisional parameters, etc. in our calculations according to that previously done in high-pressure gases [58]. We maintain the same input powers (in terms of the critical power) in all calculations ($7P_{cr}$ for $\lambda = 4$ μm and $4P_{cr}$ for $\lambda = 6$, 8, and 10 μm). Since low fractional densities yield high critical powers and hence more plasma at the beginning of propagation, the input beam waist is increased, which keeps input plasma densities low enough to prevent initial defocusing. Increasing the beam waist leads to a longer self-focusing length compared to the dispersion length, so the input pulse duration is increased for lower fractional densities to allow for filament formation. Lower densities also require longer propagation lengths due to longer self-focusing lengths. Table I summarizes some important parameters in the variable-density calculations. We also make calculations without collisional effects (ionization and absorption) to test their role.

Peak intensities versus propagation distance with different molecular densities are shown in Fig. 25, and peak plasma densities versus propagation distance are shown in Fig. 26, both with and without collisional effects (ionization and absorption). For each case filamentation occurs, but with lower peak intensities and peak plasma densities at lower molecular densities. When collisional ionization/absorption is turned off, the peak intensity increases and the peak plasma density decreases for each case. However, at low molecular densities, the effect of collisional ionization/absorption is less pronounced, yielding similar peak intensities and peak plasma densities regardless of collisional ionization/absorption. Variable molecular density calculations of maximum peak plasma densities over the entire propagation distance are shown for $\alpha = 1$, 0.5, 0.1 and 0.05 in Fig. 27(a), (b), (c) and (d), respectively. In contrast to the non-monotonic plasma-wavelength scaling with $\alpha = 1$, when the molecular density is decreased enough, plasma density decreases monotonically with wavelength, as shown in Fig. 27(c) and (d) for $\alpha = 0.1$ and 0.05, respectively. We attribute this to the lack of high-frequency bursts with low molecular densities, which will be discussed later. Comparing Fig. 27(a) to Figs. 27(b − d) also shows that collisional ionization/absorption affects plasma generation much more if $\alpha = 1$ compared to $\alpha < 1$. For example, with $\alpha = 1$ at $\lambda = 6$ μm, the difference in peak plasma density between the case with collisional ionization/absorption on versus off is $\sim 78\%$ of the value with collisional ionization/absorption on, whereas with $\alpha = 0.05$ the difference is $\sim 3\%$.

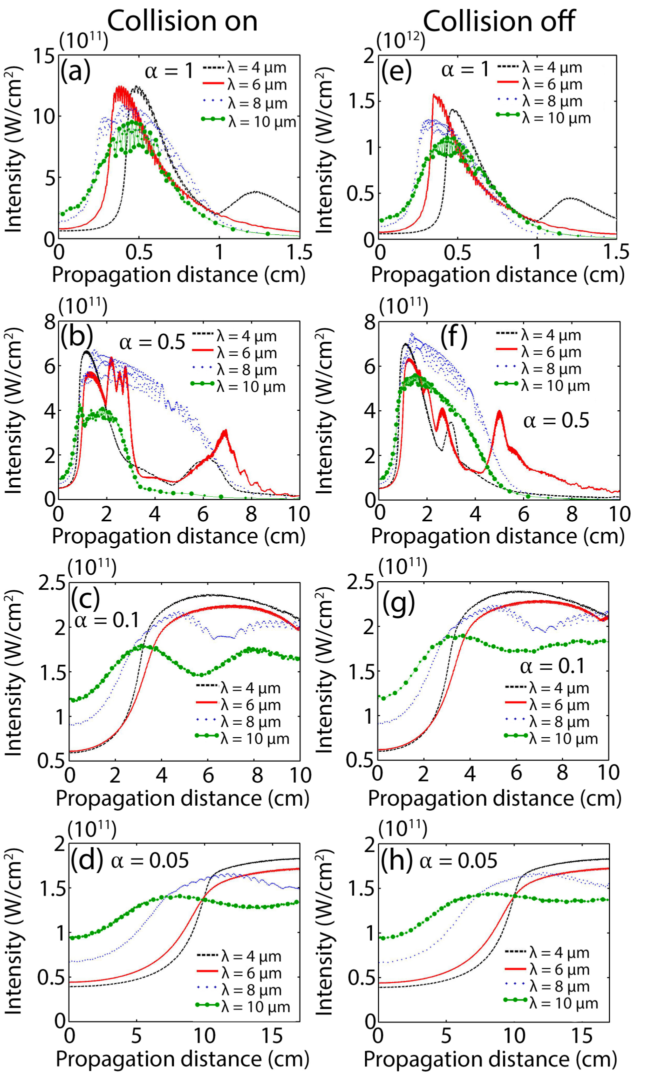

FIG. 25. (color online) Peak intensities versus propagation distance are shown with collisional ionization/absorption turned on (a − d) and off (e − h), and fractional density coefficient α set to (a, e) $\alpha = 1$, (b, f) $\alpha = 0.5$, (c, g) $\alpha = 0.1$, and (d, h) $\alpha = 0.05$. Results are shown for central wavelengths of $\lambda = 4$ (black dashed lines), $\lambda = 6$ (red solid lines), $\lambda = 8$ (blue dotted lines), and $\lambda = 10$ μm (green solid lines with circles).

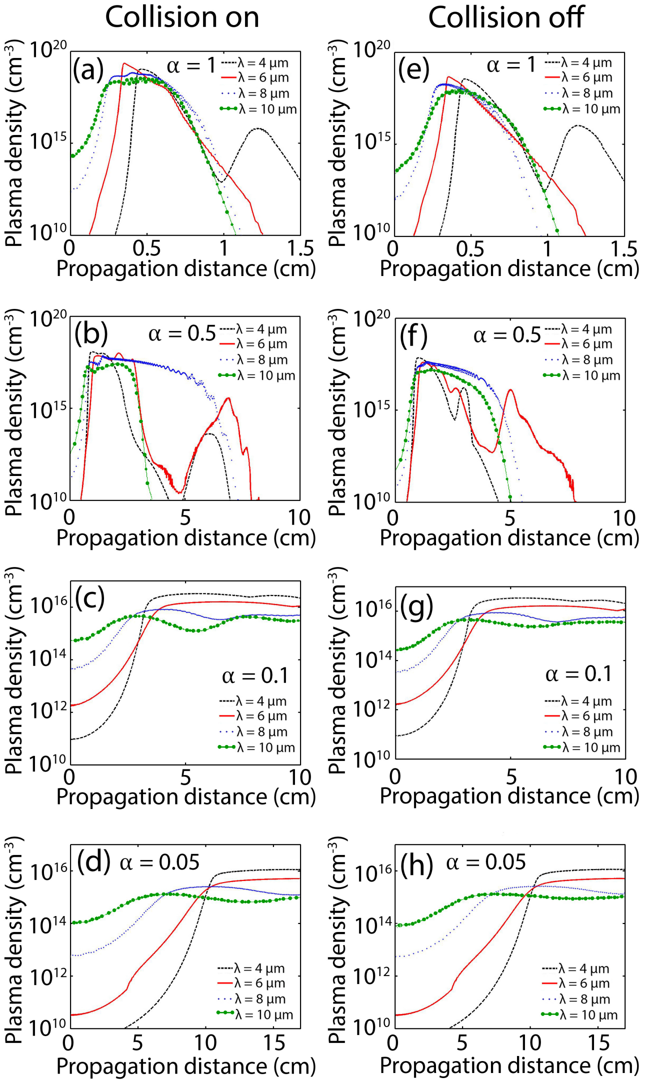

FIG. 26. (color online) Peak plasma densities versus propagation distance are shown with collisional ionization/absorption turned on (a − d) and off (e − h), and fractional density coefficient α set to (a, e) $\alpha = 1$, (b, f) $\alpha = 0.5$, (c, g) $\alpha = 0.1$, and (d, h) $\alpha = 0.05$. Results are shown for central wavelengths of $\lambda = 4$ (black dashed lines), $\lambda = 6$ (red solid lines), $\lambda = 8$ (blue dotted lines), and $\lambda = 10$ μm (green solid lines with circles).

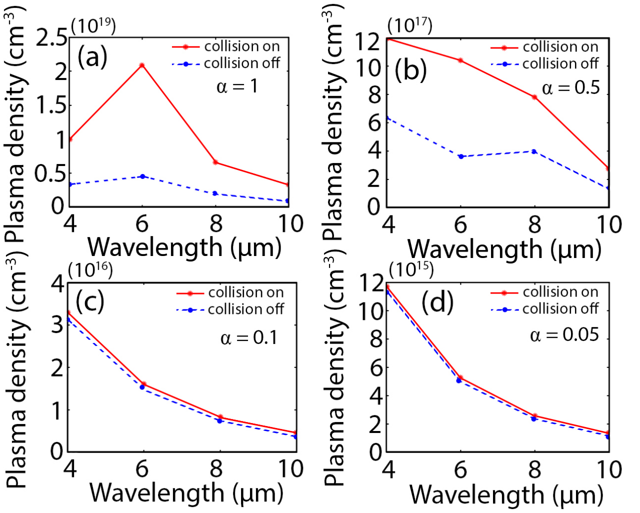

FIG. 27. (color online) Maximum plasma densities versus wavelength are shown with fractional density coefficient α and collisional ionization/absorption turned on (solid red lines, stars) and off (dashed blue lines, solid circles) for (a) $\alpha = 1$, (b) $\alpha = 0.5$, (c) $\alpha = 0.1$, and (d) $\alpha = 0.05$.

To compare the frequency content of pulses in the main calculations (high density) to low-density calculations, we carry out instantaneous frequency and XFROG calculations at each wavelength with $\alpha = 0.05$, at locations of highest plasma density. Figure 28 shows these calculation results, which can be directly compared with Fig. 24 for the main calculations. As shown by the fields in Fig. 28(a), (d), (g) and (j) and the temporal phase in Fig. 28(b), (e), (h) and (k) of each pulse, there are no apparent high-frequency bursts at any wavelength with $\alpha = 0.05$. In particular, with $\alpha = 0.05$ the central wavelength at the FWHM intensity position of the trailing edge of the 6-μm pulse is 5.6 μm, while for the 4-μm pulse the central wavelength at the trailing edge is 3.71 μm. This is made visually clear by comparing the XFROG spectrogram at 6-μm for the main calculations [Fig. 24(f)], which shows a high-frequency lobe, to the 6-μm XFROG spectrogram with $\alpha = 0.05$ [Fig. 28(f)], which does not have a high-frequency lobe. Therefore, since high-frequency bursts do not occur with $\alpha = 0.05$, we do not have non-monotonic plasma density scaling with wavelength at this low density, in contrast to the main calculations.

We conclude that the non-monotonic plasma scaling with wavelength as seen in our main calculations is mainly due to the high-frequency bursts caused by high intensities and self-steepening occurring in high-density ZnSe, and in particular the role of collisional ionization/absorption is enhanced at this high density. With low densities, high-frequency bursts do not occur, yielding monotonic scaling of plasma density with wavelength. Also note that the dispersion effect is proportional to the medium density.

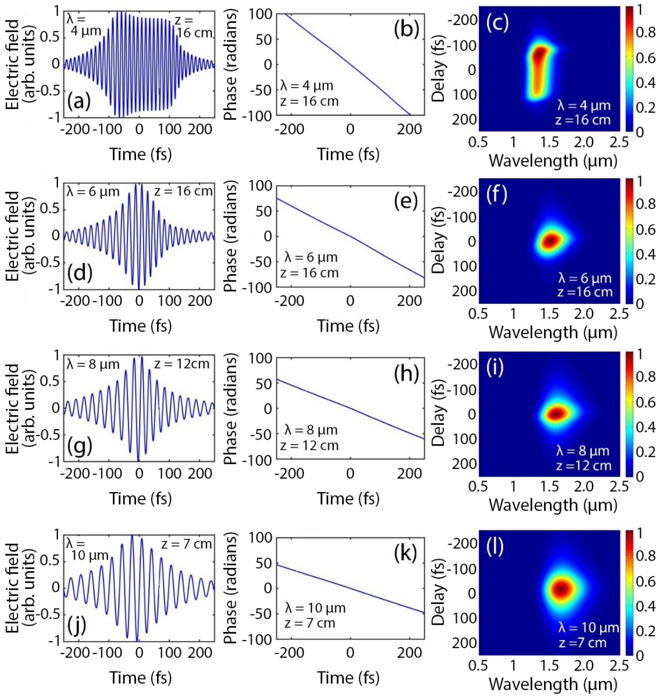

FIG. 28. (color online) Calculations are shown here with low molecular densities ($\alpha = 0.05$). On-axis normalized electric field temporal profiles are shown at labeled positions of maximum plasma density with central wavelengths of (a) $\lambda = 4$, (d) $\lambda = 6$, (g) $\lambda = 8$ and (j) $\lambda = 10$ μm. The temporal phase of each field is shown for each central wavelength in (b) $\lambda = 4$, (e) $\lambda = 6$, (h) $\lambda = 8$ and (k) $\lambda = 10$ μm. Corresponding XFROG spectrograms are shown for central wavelengths of (c) $\lambda = 4$, (f) $\lambda = 6$, (i) $\lambda = 8$ and (l) $\lambda = 10$ μm. Here the delay axis corresponds to the offset between the reference pulse and the signal pulse (to be analyzed), where a delay of 0 fs means the reference field at 0 fs is overlapped with the signal field at 0 fs.

APPENDIX D: ENVELOPE INTERPOLATION OVER CARRIER OSCILLATIONS

Since the UPPE is carrier-resolved the modeled pulses contain fast oscillations with periods at the carrier cycle. To retrieve the intensity envelope, we interpolate the carrier-resolved intensity. Envelope-interpolated versions of Figs. 7, 9, 11, 12 and 19 are shown in Figs. 29, 30, 31, 32 and 33, respectively. Oscillations shown in Fig. 3 are numerical artifacts that occur due to a mismatch between the group velocities and phase velocities at each wavelength, causing carrier-envelope phase drifts and varying peak intensities.

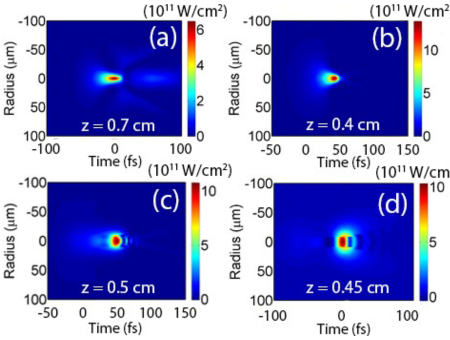

FIG. 29. (color online) An envelope-interpolated version of Fig. 7: spatio-temporal intensity profiles at labeled propagation distances of shortest pulse duration are shown for (a) $\lambda = 4$, (b) $\lambda = 6$, (c) $\lambda = 8$, and (d) $\lambda = 10$ μm. The color bars show intensity in W/cm^2

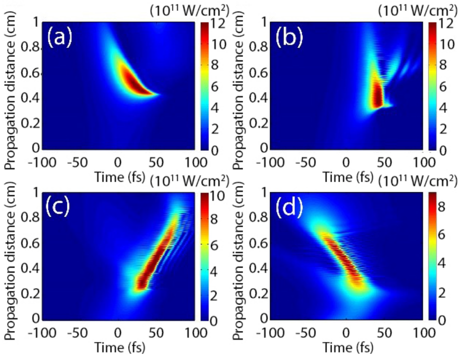

FIG. 30. (color online) An envelope-interpolated version of Fig. 9: on-axis temporal profiles versus propagation distance are shown for (a) $\lambda = 4$, (b) $\lambda = 6$, (c) $\lambda = 8$, and (d) $\lambda = 10$ μm. The color bars show intensity in W/cm^2.

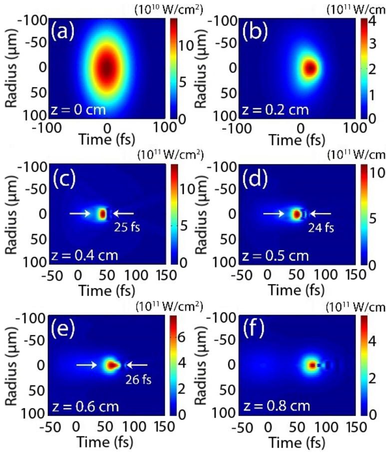

FIG. 31. (color online) An envelope-interpolated version of Fig. 11: spatio-temporal intensity profiles are shown for $\lambda = 8$ μm at (a) $z = 0$, (b) $z = 0.2$, (c) $z = 0.4$, (d) $z = 0.5$, (e) $z = 0.6$, and (f) $z = 0.8$ cm. A light bullet persists from $z = 0.4$ to $z = 0.6$ cm. The color bars show intensity in W/cm^2, and spatially-averaged pulse durations are labeled with arrows where light bullets propagate.

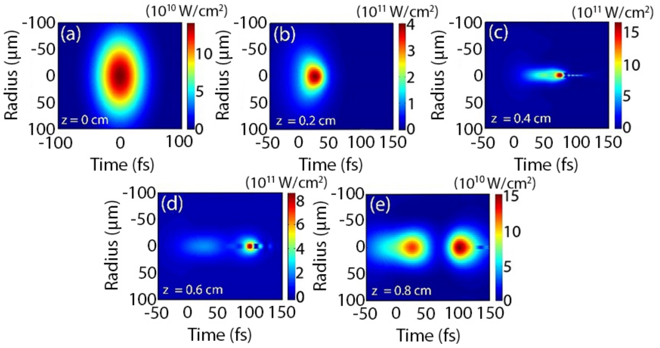

FIG. 32. (color online) An envelope-interpolated version of Fig. 12: spatio-temporal intensity profiles are shown with $\lambda = 8$ μm and an input power of $4P_{cr}$ at propagation distances of (a) $z = 0$, (b) $z = 0.2$, (c) $z = 0.4$, (d) $z = 0.6$, and (e) $z = 0.8$ cm, as labeled. Here plasma effects are turned off. The color bars show intensity in W/cm^2.

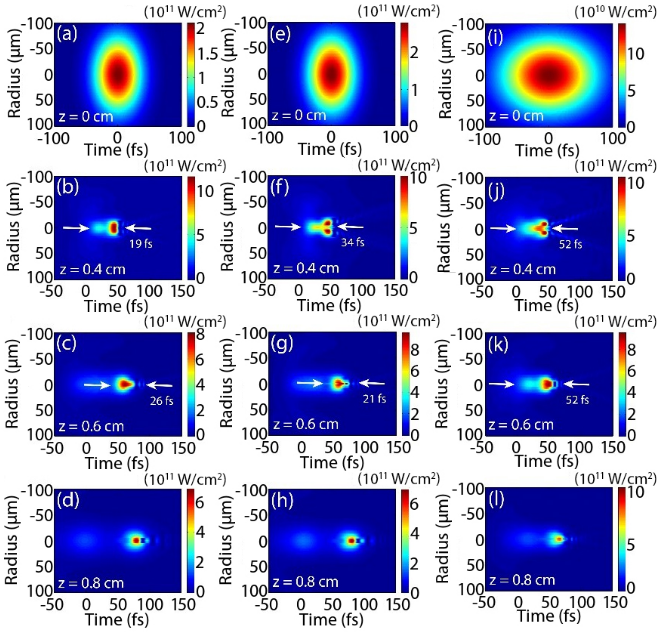

FIG. 33. (color online) An envelope-interpolated version of Fig. 19: spatio-temporal intensity profiles are shown for $\lambda = 8$ μm at labeled propagation distances with input powers and input FWHM pulse durations of (a $-$ d) $6P_{cr}$, 60 fs, (e $-$ h) $8P_{cr}$, 60 fs, and (i $-$ l) $4P_{cr}$, 120 fs. The color bars show intensity in W/cm^2, and selected spatially-averaged pulse durations are labeled with arrows.

---

[1] A. Braun, G. Korn, X. Liu, D. Du, J. Squier, and G. Mourou, Opt. Lett. **20**, 73 (1995).

[2] S. L. Chin, S. A. Hosseini, W. Liu, Q. Luo, F. Théberge, N. Aközbek, A. Becker, V. P. Kandidov, O. G. Kosareva, and H. Schroeder, Can. J. Phys. **83**, 863 (2005).

[3] A. Couairon and A. Mysyrowicz, Phys. Rep. **441**, 47 (2007).

[4] L. Bergé, S. Skupin, R. Nuter, J. Kasparian, and J.-P. Wolf, Rep. Prog. Phys. **70**, 1633 (2007).

[5] A. D. DiChiara, S. Ghimire, C. I. Blaga, E. Sistrunk, E. P. Power, A. M. March, T. A. Miller, D. A. Reis, P. Agostini, and L. F. DiMauro, IEEE J. Sel. Topics Quantum Electron. **18**, 419 (2012).

[6] G. Andriukaitis, T. Balčiūnas, S. Ališauskas, A. Pugžlys, A. Baltuška, T. Popmintchev, M.-C. Chen, M. M. Murnane, and H. C. Kapteyn, Opt. Lett. **36**, 2755 (2011).

[7] A. Thai, M. Hemmer, P. K. Bates, O. Chalus, and J. Biegert, Opt. Lett. **36**, 3918 (2011).

[8] H. Liang, D. L. Weerawarne, P. Krogen, R. I. Grynko, C.-J. Lai, B. Shim, F. X. Kärtner, and K.-H. Hong, Optica **3**, 678 (2016).

[9] Y. Yin, A. Chew, X. Ren, J. Li, Y. Wang, Y. Wu, and Z. Chang, Sci. Rep. **7**, 45794 (2017).

[10] G. Fibich and A. L. Gaeta, Opt. Lett. **25**, 335 (2000).

[11] P. Colosimo, G. Doumy, C. I. Blaga, J. Wheeler, C. Hauri, F. Catoire, J. Tate, R. Chirla, A. M. March, G. G. Paulus, H. G. Muller, P. Agostini, and L. F. DiMauro, Nature Phys. **4**, 386 (2008).

[12] Z. Chang, P. B. Corkum, and S. R. Leone, J. Opt. Soc. Am. B **33**, 1081 (2016).

[13] T. Popmintchev, M.-C. Chen, D. Popmintchev, P. Arpin, S. Brown, S. Ališauskas, G. Andriukaitis, T. Balčiunas, O. D. Mücke, A. Pugzlys, A. Baltuška, B. Shim, S. E. Schrauth, A. Gaeta, C. Hernández-García, L. Plaja, A. Becker, A. Jaron-Becker, M. M. Murnane, and H. C. Kapteyn, Science **336**, 1287 (2012).

[14] S. Ghimire, A. D. DiChiara, E. Sistrunk, P. Agostini, L. F. DiMauro, and D. A. Reis, Nature Phys. **7**, 138 (2011).

[15] Y. S. You, D. A. Reis, and S. Ghimire, Nature Phys. **13**, 345 (2017).

[16] C. Hernández-García, J. A. Pérez-Hernández, T. Popmintchev, M. M. Murnane, H. C. Kapteyn, A. Jaron-Becker, A. Becker, and L. Plaja, Phys. Rev. Lett. **111**, 033002 (2013).

[17] L. Bergé, J. Rolle, and C. Köhler, Phys. Rev. A **88**, 023816 (2013).

[18] P. Panagiotopoulos, P. Whalen, M. Kolesik, and J. V. Moloney, Nat. Photon. **9**, 543 (2015).

[19] P. Whalen, P. Panagiotopoulos, M. Kolesik, and J. V. Moloney, Phys. Rev. A **89**, 023850 (2014).

[20] P. Panagiotopoulos, K. Schuh, M. Kolesik, and J. V. Moloney, J. Opt. Soc. Am. B **33**, 2154 (2016).

[21] J. P. Palastro, J. Peñano, L. A. Johnson, B. Hafizi, J. K. Wahlstrand, and H. M. Milchberg, Phys. Rev. A **94**, 023816 (2016).

[22] B. Shim, S. E. Schrauth, and A. L. Gaeta, Opt. Express **19**, 9118 (2011).

[23] Y. E. Geints and A. A. Zemlyanov, J. Opt. Soc. Am. B **31**, 788 (2014).

[24] K. Schuh, M. Kolesik, E. M. Wright, J. V. Moloney, and S. W. Koch, Phys. Rev. Lett. **118**, 063901 (2017).

[25] Y. Silberberg, Opt. Lett. **15**, 1282 (1990).

[26] B. A. Malomed, D. Mihalache, F. Wise, and L. Torner, J. Opt. B **7**, R53 (2005).

[27] M. Durand, A. Jarnac, A. Houard, Y. Liu, S. Grabielle, N. Forget, A. Durécu, A. Couairon, and A. Mysyrowicz, Phys. Rev. Lett. **110**, 115003 (2013).

[28] D. Majus, G. Tamošauskas, I. Gražulevičiūtė, N. Garejev, A. Lotti, A. Couairon, D. Faccio, and A. Dubietis, Phys. Rev. Lett. **112**, 193901 (2014).

[29] C. Brée, I. Babushkin, U. Morgner, and A. Demircan, Phys. Rev. Lett. **118**, 163901 (2017).

[30] A. A. Voronin and A. M. Zheltikov, Sci.Rep. **7**, 36263 (2017).

[31] A. M. Zheltikov, J. Phys. B **50**, 092001 (2017).

[32] F. Silva, D. R. Austin, A. Thai, M. Baudisch, M. Hemmer, D. Faccio, A. Couairon, and J. Biegert, Nat. Commun. **3**, 807 (2012).

[33] V. Shumakova, P. Malevich, S. Ališauskas, A. Voronin, A. M. Zheltikov, D. Faccio, D. Kartashov, A. Baltuška, and A. Pugžlys., Nat. Commun. **7**, 12877 (2016).

[34] H. Liang, P. Krogen, R. Grynko, O. Novak, C.-L. Chang, G. J. Stein, D. Weerawarne, B. Shim, F. X. Kärtner, and K.-H. Hong, Opt. Lett. **40**, 1069 (2015).

[35] E. A. Stepanov, A. A. Lanin, A. A. Voronin, A. B. Fedotov, and A. M. Zheltikov, Phys. Rev. Lett. **117**, 043901 (2016).

[36] A. A. Voronin and A. M. Zheltikov, Phys. Rev. A **94**, 023824 (2016).

[37] M. Durand, A. Houard, K. Lim, A. Durécu, O. Vasseur, and M. Richardson, Opt. Express **22**, 5852 (2014).

[38] O. Mouawad, P. Béjot, F. Billard, P. Mathey, B. Kibler, F. Désévédavy, G. Gadret, J.-C. Jules, O. Faucher, and F. Smektala, Opt. Mater. **60**, 355 (2016).

[39] R. Šuminas, G. Tamošauskas, G. Valiulis, V. Jukna, A. Couairon, and A. Dubietis, Appl. Phys. Lett. **110**, 241106 (2017).

[40] M. Kolesik and J. V. Moloney, Phys. Rev. E **70**, 036604 (2004).

[41] A. Couairon, E. Brambilla, T. Corti, D. Majus, O. de J. Ramírez-Góngora, and M. Kolesik, Eur. Phys. J. Special Topics **199**, 5 (2011).

[42] R. I. Grynko, D. L. Weerawarne, and B. Shim, Phys. Rev. A **96**, 013816 (2017).

[43] T. D. Krauss and F. W. Wise, Appl. Phys. Lett. **65**, 1739 (1994).

[44] N. Sarmadian, R. Saniz, B. Partoens, and D. Lamoen, J. Appl. Phys. **120**, 085707 (2016).

[45] L. V. Keldysh, Sov. Phys. JETP **20**, 1307 (1965).

[46] L. Quiroga, F. J. Rodríguez, A. Camacho, and C. Tejedor, Phys. Rev. B **42**, 11198 (1990).

[47] P. Balling and J. Schou, Rep. Prog. Phys. **76**, 036502 (2013).

[48] Y. E. Geints and A. A. Zemlyanov, Appl. Opt. **56**, 1397 (2017).

[49] P. Panagiotopoulos, P. Whalen, M. Kolesik, and J. V. Moloney, J. Opt. Soc. Am. B **32**, 1718 (2015).

[50] A. V. Husakou and J. Herrmann, Phys. Rev. Lett. **87**, 203901 (2001).

[51] M. Conforti, A. Marini, T. X. Tran, D. Faccio, and F. Biancalana, Opt. Express **21**, 31239 (2013).

[52] S. Skupin, G. Stibenz, L. Bergé, F. Lederer, T. Sokollik, M. Schnürer, N. Zhavoronkov, and G. Steinmeyer, Phys. Rev. E **74**, 056604 (2006).

[53] L. Bergé, Opt. Express **16**, 21529 (2008).

[54] L. Bergé, C.-L. Soulez, C. Köhler, and S. Skupin, Appl. Phys. B **103**, 563 (2011).

[55] A. H. Chin, O. G. Calderón, and J. Kono, Phys. Rev. Lett. **86**, 3292 (2001).

[56] G. Agrawal, *Nonlinear Fiber Optics* (Academic Press, 1989).

[57] S. Linden, H. Giessen, and J. Kuhl, Phys. Status Solidi B **206**, 119 (1998).

[58] M. Mlejnek, E. M. Wright, and J. V. Moloney, Phys. Rev. E **58**, 4903 (1998).